Lithos 109 (2009) 1-22

Contents lists available at ScienceDirect

Lithos

journal homepage: www.elsevier.com/locate/lithos

The elusive lithosphere–asthenosphere boundary (LAB) beneath cratons

David W. Eaton [a,*], Fiona Darbyshire [b], Rob L. Evans [c], Herman Grütter [d], Alan G. Jones [e], Xiaohui Yuan [f]

[a] Department of Geoscience, University of Calgary, Calgary, Alberta, Canada T2N 1N4
[b] GEOTOP UQÀM-McGill, Université du Québec à Montréal, Canada H3C 3P8
[c] Department of Geology and Geophysics, Woods Hole Oceanographic Institution, Woods Hole, Massachusetts 02543, USA
[d] BHP Billiton World Exploration Inc., Suite 800, Four Bentall Centre, 1055 Dunsmuir Street, Vancouver, B.C., Canada V7X 1L2
[e] Dublin Institute for Advanced Studies, 5 Merrion Square, Dublin 2, Ireland
[f] GeoForschungsZentrum, Telegrafenberg, D-14473 Potsdam, Germany

ARTICLE INFO

Article history:
Received 19 March 2008
Accepted 21 May 2008
Available online 5 June 2008

Keywords:
Petrologic lithosphere
Thermal lithosphere
Seismic lithosphere
Electrical lithosphere
Craton

ABSTRACT

The lithosphere–asthenosphere boundary (LAB) is a first-order structural discontinuity that accommodates differential motion between tectonic plates and the underlying mantle. Although it is the most extensive type of plate boundary on the planet, its definitive detection, especially beneath cratons, is proving elusive. Different proxies are used to demarcate the LAB, depending on the nature of the measurement. Here we compare interpretations of the LAB beneath three well studied Archean regions: the Kaapvaal craton, the Slave craton and the Fennoscandian Shield. For each location, xenolith and xenocryst thermobarometry define a mantle stratigraphy, as well as a steady-state conductive geotherm that constrains the minimum pressure (depth) of the base of the thermal boundary layer (TBL) to 45–65 kbar (170–245 km). High-temperature xenoliths from northern Lesotho record Fe-, Ca- and Ti-enrichment, grain-size reduction and globally unique supra-adiabatic temperatures at 53–61 kbar (200–230 km depth), all interpreted to result from efficient advection of asthenosphere-derived melts and heat into the TBL. Using a recently compiled suite of olivine creep parameters together with published geotherms, we show that beneath cratons the probable deformation mechanism near the LAB is dislocation creep, consistent with widely observed seismic and electrical anisotropy fabrics. If the LAB is dry, it is probably diffuse (>50 km thick) and high levels of shear stress (>2 MPa or >20 bar) are required to accommodate plate motion. If the LAB is wet, lower shear stress is required to accommodate plate motion and the boundary may be relatively sharp (≤20 km thick).
The seismic LAB beneath cratons is typically regarded as the base of a high-velocity mantle lid, although some workers infer its location based on a distinct change in seismic anisotropy. Surface-wave inversion studies provide depth-constrained velocity models, but are relatively insensitive to the sharpness of the LAB. The *S*-receiver-function method is a promising new seismic technique with complementary characteristics to surface-wave studies, since it is sensitive to sharpness of the LAB but requires independent velocity information for accurate depth estimation. Magnetotelluric (MT) observations have, for many decades, imaged an "electrical asthenosphere" layer at depths beneath the continents consistent with seismic low-velocity zones. This feature is most easily explained by the presence of a small amount of water in the asthenosphere, possibly inducing partial melt. Depth estimates based on various proxies considered here are similar, lending confidence that existing geophysical tools are effective for mapping the LAB beneath cratons.

1. Introduction

The *lithosphere* is a rigid mechanical boundary layer at the Earth's surface. It is underlain by a weak layer (the *asthenosphere*), which is characterised by pervasive plastic deformation (solid-state creep) on time scales of tens of thousands of years. The rheological concepts of lithosphere and asthenosphere originated from studies of post-glacial rebound (Barrell, 1914), but have since been incorporated into the plate-tectonic paradigm as fundamental components. In this paradigm, the lithosphere is composed of discrete plates and the lithosphere–asthenosphere boundary (LAB) separates each plate from the underlying convecting mantle. The LAB thus constitutes a detachment zone that comprises the most extensive type of plate boundary on the planet, underlying both oceanic and continental regions.

Although the LAB is an active plate boundary, beneath the continents it is relatively cryptic compared to other first-order structural subdivisions of the Earth. Specimens of the LAB and environs, in the form of xenoliths and xenocrysts brought to the surface in alkaline magmas such as *kimberlite*, are sparsely and unevenly distributed and,

* Corresponding author. Tel.: +1 403 220 4275; fax: +1 403 284 0074.
E-mail address: eatond@ucalgary.ca (D.W. Eaton).

0024-4937/$ – see front matter © 2008 Elsevier B.V. All rights reserved.
doi:10.1016/j.lithos.2008.05.009

as argued below, virtually nonexistent beneath cratons. Furthermore, since the differential motion between lithosphere and asthenosphere is generally accommodated aseismically, there is no seismological technique to map the LAB directly. In addition, global gravity observations show that the lithosphere is approximately in large-scale isostatic equilibrium (Shapiro et al., 1999), rendering long-wavelength gravity inversion ineffective as a mapping tool. These limitations have spawned many indirect proxies for the LAB (Fig. 1) that depend, in a practical sense, on the type of measurement made. These proxies are derived from disparate types of observations, including petrologic, geochemical, thermal, seismic-velocity, seismic-anisotropy and electrical-conductivity characteristics of the LAB and regions directly above and below it.

Various lines of evidence (e.g., Jordan, 1975, 1978; Hoffman, 1990; Forte and Perry, 2001) suggest that the lithosphere is thickest, strongest and most refractory within the ancient (>1 Ga) nuclei of continents (*cratons*). Mapping the LAB beneath cratons is important, since it is an essential constraint for models of the formation and evolution of continents. Moreover, thick lithospheric roots (sometimes referred to as *tectosphere*) beneath cratons appear to exhibit large variations in thickness (Artemieva and Mooney, 2002) and are likely to represent areas where the plates are most strongly coupled to mantle flow (Conrad and Lithgow-Bertelloni, 2006). Consequently, detailed models of mantle convection depend on accurate knowledge of the topology of the LAB. Finally, the continental-scale distribution of scientifically and economically important diamondiferous kimberlites may be partly controlled by the LAB topology (Griffin et al., 2004) and deep structure within the lithosphere (Stubley, 2004).

The LAB is particularly elusive in cratonic regions. Every proxy for inferring the character and depth of the LAB comes with its own set of assumptions and limitations, and the relationships between the different proxies are controversial and poorly understood. The purpose of this paper is to review and attempt to understand the difference between results from a number of widely used methods to characterise the LAB. We focus on three well studied Archean cratons in southern Africa, northern Canada and Finland, respectively (Fig. 2), where the LAB has been investigated independently using several different methods. The objectives of this study are:

1) to evaluate critically a number of widely used proxies for the LAB;
2) to compare these proxies with each other and with realistic rheological models of the "true" (i.e., mechanical) lithosphere; and,
3) to assess the extent to which different techniques sense the same feature, and if so, to document its intrinsic characteristics.

The paper is organized into sections covering the *petrologic* LAB and *thermal boundary layer* (TBL), based on xenolith and xenocryst data; the *rheological* LAB, based on numerical modelling of mantle creep and stress regime; the *seismological* LAB, based mainly on studies of surface waves and *S*-receiver functions; and the *electrical* LAB, based on *magnetotelluric* surveys. Since this work is, of necessity, highly multidisciplinary, terms that are italicized on first use are defined in the following glossary.

2. Glossary

2.1. Adiabat

An idealised curve in *P–T* space describing a state in which heat is neither gained nor lost. The adiabat is parameterised by its potential temperature, the temperature that would be attained by a parcel of

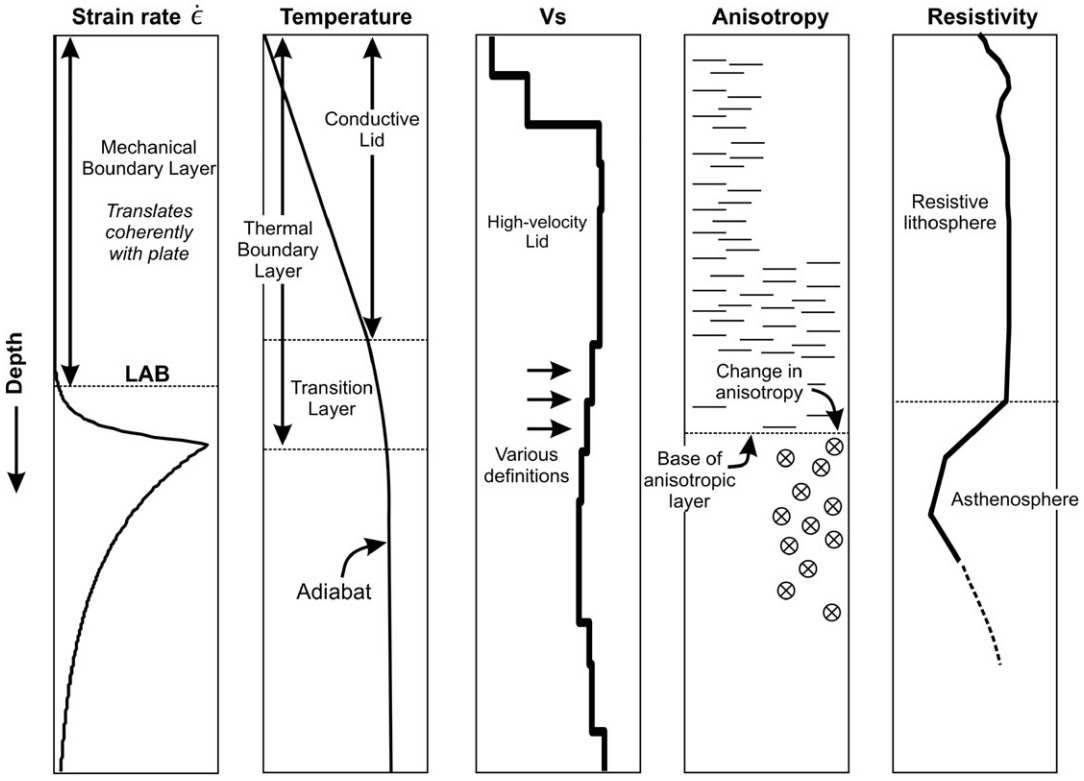

Fig. 1. Definition of the lithosphere and common proxies used to estimate its thickness. The lithosphere, *sensu stricto*, is a mechanical boundary layer (left). The lithosphere–asthenosphere boundary (LAB) coincides with the top of a zone of decoupling between the lithosphere and asthenosphere, marked by an increased strain rate. The thermal boundary layer (TBL), containing a conductive lid and a transition layer, represents a near-surface region where temperature deviates from the adiabat. A zone of low seismic shear-wave velocity (Vs) is sometimes detected beneath a high-velocity lid; various definitions have been used to correlate this zone with the LAB (see text). The LAB may also correlate with a downward extinction of seismic anisotropy (e.g., Gaherty and Jordan, 1995) or a change in the direction of anisotropy (e.g., Debayle and Kennett, 2000a; 2000b; Sebai et al., 2006). The electrical LAB is marked by a significant reduction in electrical resistivity.

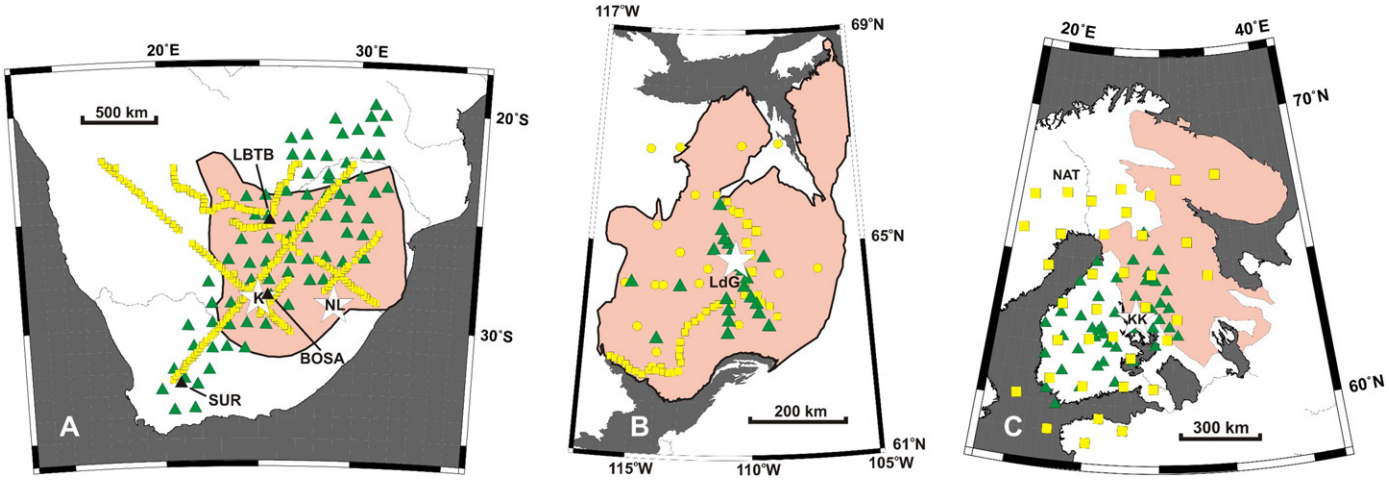

Fig. 2. Location maps for the three cratons considered in this study. Triangles denote broadband seismic stations, squares and circles denote magnetotelluric (MT) observatories, and stars denote kimberlite localities. A. Kaapvaal craton, southern Africa, showing location of seismic (SASE) and MT (SAMTEX) experiments (Hamilton et al., 2006) as well as stations SUR, BOSA and LBTB used for S-receiver functions. NL, K denote northern Lesotho and Kimberley, respectively. B. Slave craton, northern Canada, showing location of seismic (POLARIS; Chen et al., 2007) and MT (Lithoprobe; Jones et al., 2001) experiments. LdG denotes Lac de Gras. C. Archean domains of Fennoscandia, including Karelian craton and Lapland-Kola domain, showing location of the seismic (SVEKALAPKO; Bruneton et al., 2004a) and MT (BEAR; Engels et al., 2002) experiments. KK denotes Kuopio-Kaavi kimberlites. NAT denotes MT observatory used in Fig. 13.

material if brought adiabatically to a pressure of 1 bar (0.1 MPa) without melting.

2.2. Asthenosphere

A rheological term referring to the weak mantle layer below the lithosphere.

2.3. Azimuthal anisotropy

A term that denotes a type of *seismic anisotropy* in which velocity is dependent on either propagation direction (often mapped using surface waves), polarization (often mapped using SKS splitting observations) or both.

2.4. Chemical boundary layer

The part of the upper mantle that is intrinsically strong as a result of melt depletion and dehydration. The presence of this layer may regulate the thickness of the thermal boundary layer (Lee et al., 2005).

2.5. Conductive geotherm

A temperature profile in the Earth that reflects a state in which heat is transferred to Earth's surface by diffusion from the hot interior. Internal heating is also supplied by radioactive decay. A conductive geotherm is mainly parameterized by its heat flow, typically measured in mW/m^2, but depth profiles of internal heat generation and thermal conductivity are also required to calculate the geotherm.

2.6. Craton

The core region of a continent that has remained stable on a billion-year (Ga) time scale (Hoffman, 1988). This term also denotes large Archean domains, such as the Kaapvaal craton, as distinct from adjacent younger mobile belts. In this paper, when the term craton is used without a qualifier the first meaning is implied.

2.7. Diffusion creep

A mode of subsolidus deformation that occurs through diffusive mass transport at the molecular level between grain boundaries. Strain rate is proportional to shear stress (also known as a linear Newtonian rheology) and approximately inversely proportional to the cube of average grain size. Diffusion creep does not produce *lattice-preferred orientation*.

2.8. Dislocation creep

A mode of subsolidus deformation that occurs through the motion of crystalline dislocations within grains. Strain rate is a highly nonlinear function of shear stress and independent of average grain size. Dislocation creep leads to lattice–preferred orientation.

2.9. Elastic lithosphere

The mechanically strong outer shell of the Earth that can support applied loads elastically and without permanent deformation. Since all rocks are viscoelastic, that is, they behave like elastic solids under short duration of stress, but can creep if the duration of the loading exceeds the Maxwell Time (equal to the viscosity of the rock divided by its elastic moduli), the effective thickness of the elastic lithosphere depends on the residence time of the load.

2.10. Electrical asthenosphere

A conductive layer in the upper mantle often identified to coincide with a seismic low-velocity zone.

2.11. Electrical lithosphere

The outer, generally electrically resistive, layer of the Earth that coincides approximately with the lithosphere.

2.12. FO

A bulk depletion index given by 100Mg/(Mg+Fe) in olivine. Fertile asthenosphere has FO89, depleted lithosphere ranges up to FO95.

2.13. G9 and G10 garnets

Normal and low-calcium garnets used as indicators of diamondiferous kimberlites. Originally defined by Gurney (1984) based on a calcium–chrome ($CaO–Cr_2O_3$) cross-plot, this classification scheme has been refined recently by Grütter et al. (2004). A crossplot relating olivine FO to G9 and G10 garnet compositions is introduced in Fig. 4 of this work.

2.14. Kimberlite

A rare ultramafic igneous rock of mantle origin. Its low magmatic *viscosity* enables very rapid ascent through the lithosphere, allowing it to entrain diamonds and bring them to the surface without retrogressing to graphite.

2.15. Lattice-preferred orientation (LPO)

Also known as crystallographic preferred orientation, LPO is a microfabric caused by alignment of anisotropic mineral grains such that common crystallographic axes are roughly aligned.

2.16. Lehmann discontinuity

A global seismic discontinuity at approximately 220 km depth, which was originally proposed by Lehmann (1960) to be the sharp base of the asthenospheric low-velocity zone. More recently, this feature has been interpreted by Gaherty and Jordan (1995) as a rapid downward extinction of radial anisotropy.

2.17. Lithosphere

A rheological term referring to the strong outer shell of the Earth composed of the crust and upper part of the mantle; also called a mechanical boundary layer. The lithosphere is composed of individual, coherently translating plates. Its base may be sharp or diffuse.

2.18. Magnetotellurics

A geophysical technique which uses frequency dependent ratios of naturally occurring electric and magnetic fields at the surface of the Earth to determine the electrical electrical-conductivity structure at depth. Increasing depths of sensitivity are obtained by recording lower frequency fields.

2.19. Petrologic lithosphere

The melt-depleted part of the upper mantle, including deep portions that may be occupied dominantly by melt-metasomatised mantle rocks.

2.20. Radial seismic anisotropy

A term that denotes a type of seismic anisotropy detected using surface waves, in which inferred shear-wave velocity is higher for horizontally polarized Love waves (V_{SH}) than for vertically polarized Rayleigh waves (V_{SV}). This type of anisotropy is attributed by many authors to flow-induced shear in the asthenosphere.

2.21. Receiver-function method

A widely used seismic technique that isolates the near-station scattering response from source and path effects by deconvolving an observed seismogram (typically but not always the radial component), using the signal from another observed seismogram (typically the corresponding vertical component).

2.22. Rheological lithosphere

A representation of the lithosphere based on deformation rate and regime. Many previous studies (e.g., Dragoni et al., 1993) assume a uniform strain rate in order to compute a strength profile, and then define the LAB as the depth where shear strength drops below a particular value (e.g., 1 MPa). Here, we assume that stress is uniform and impose kinematic boundary conditions, based on plate motion relative to the underlying asthenosphere, to compute a strain-rate profile. We use a strain rate of 10^{-15} s^{-1} to delineate the lithosphere–asthenosphere boundary (LAB).

2.23. Seismic anisotropy

A variation in seismic wavespeed as a function of propagation direction or polarization.

2.24. Seismological lithosphere

The generally high-velocity outer layer of the Earth, approximately coincident with the lithosphere, which typically overlies a low-velocity zone. Some studies associate the LAB with a distinct change in seismic anisotropy.

2.25. Tectosphere

A term introduced by Jordan (1981) to denote mantle material that translates more-or-less coherently beneath cratons on billion-year (Ga) time scales, emphasizing the nature of continents as chemical boundary layers. The term does not connote strength and so is not equivalent to the lithosphere. Jordan (1981) proposed that the tectosphere may be considerably thicker than the lithosphere beneath cratons, up to ~400 km.

2.26. Thermal boundary layer (TBL)

A thermal transition layer at the top (or base) of a convecting system. Here, the TBL signifies a surface layer whose geotherm deviates from the adiabat.

2.27. Thermal transition layer

A term used here to signify a depth interval with a geotherm that is intermediate between conductive and adiabatic.

2.28. Viscosity

A measure of resistance of a material to flow. Viscosity exhibits the largest natural variation of any geophysical parameter, more than 30 orders of magnitude. SI units of viscosity are Pa s.

3. The xenolith and xenocryst record

Thermobarometric techniques developed for xenoliths since the mid-1970s have validated stratigraphies for cratonic lithosphere that extend to almost 250 km depth. Such stratigraphies commonly exhibit coarse-textured peridotites that equilibrated near conductive pressure–temperature conditions and are replaced at depth by high-temperature, dynamically recrystallized peridotites with finer-grained "sheared" textures (e.g., Finnerty and Boyd, 1987).

3.1. Northern Lesotho xenoliths: the thermobarometric basis for mantle stratigraphy

Mantle xenoliths from northern Lesotho (Fig. 3) provide an oft-cited type section that defines a classic stratigraphy of cratonic lithospheric mantle. In recrystallized, high-temperature peridotites at this locality, Fe/Mg-, Al/Cr- and Ca-depleted samples with typically "lithosphere-like" compositions and coarse textures are transformed to "asthenosphere-like" compositions by infiltration of Fe, Ca, Al, Ti and other incompatible elements (Smith and Boyd, 1989; Griffin et al., 1996). Most modern geobarometers predict depths for these high-temperature xenoliths that are too shallow to be compatible with a single conductive geotherm (Fig. 3; Finnerty, 1989). This suggests that these high-temperature samples have been thermally disturbed.

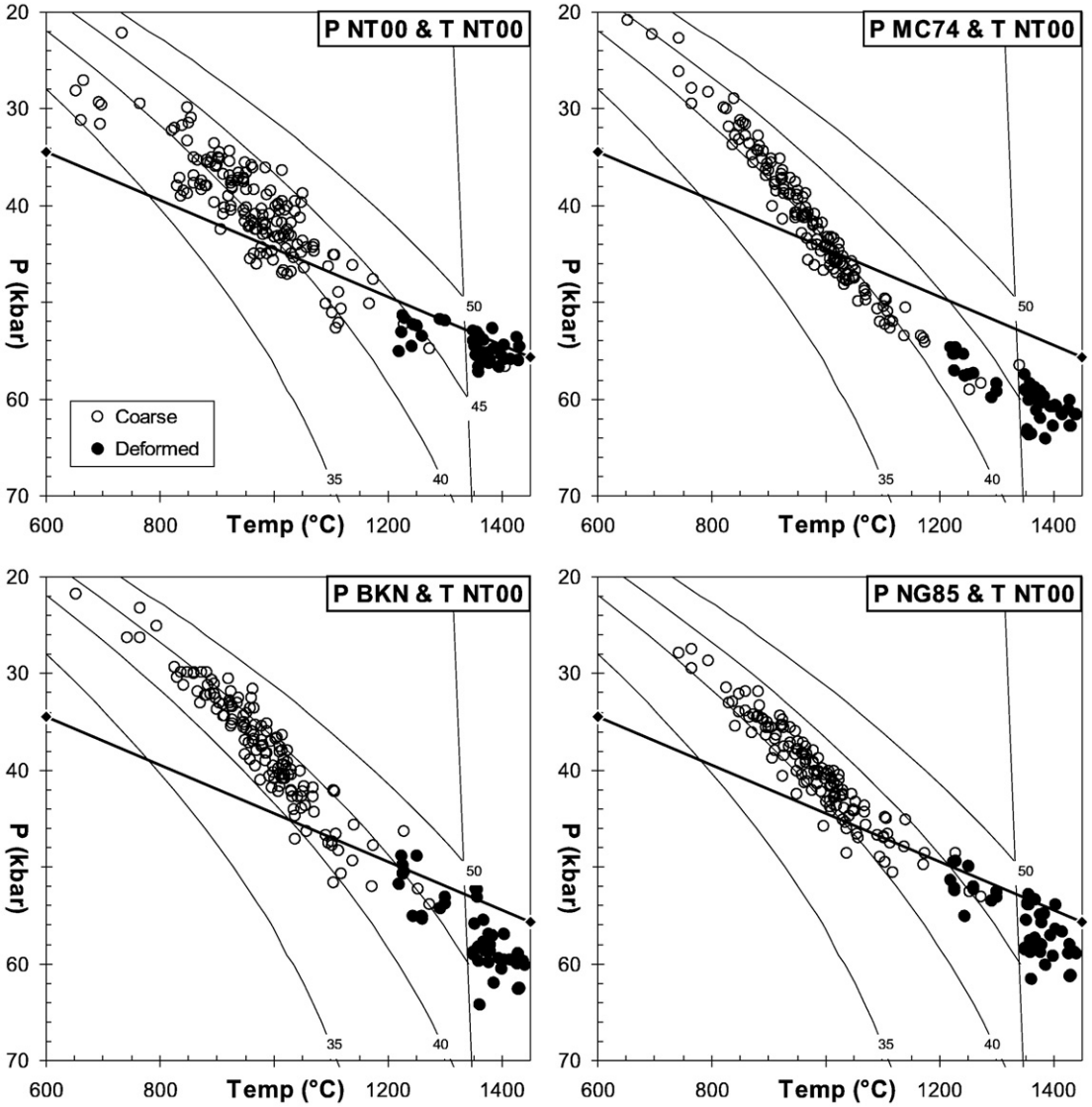

Fig. 3. Variation of thermobarometry results for garnet lherzolite xenoliths from North Lesotho kimberlites, as a function of different barometer(s) combined with the same thermometer. Pressures (*P*, kbar) are calculated using four common pyroxene-barometry formulations (abbreviated P NT00, P MC74, P BKN, P NG85) at a fixed temperature (Temp, °C) for each xenolith. For uniformity the Al,Cr-in-pyroxene barometer of Nickel and Green (1985, abbreviated P NG85) and the clinopyroxene-solvus thermometer of Nimis and Taylor (2000, abbreviated T NT00) are used in the remainder of this paper. Model conductive geotherms labelled 35, 40, 45 and 50 are after Pollack and Chapman (1977) and terminate in a mantle adiabat with Tp = 1300 °C. The graphite/diamond equilibrium (solid line terminated by diamond symbols) is that of Kennedy and Kennedy (1976). Xenolith data sources and thermobarometry techniques and abbreviations are given in Grütter and Moore (2003).

Reviews by Brey and Kohler (1990), Taylor (1998) and Smith (1999) outline a number of complications that may arise when applying thermobarometers to such xenolith suites. For example, one-sigma errors of ±3 kbar and ±50 °C are commonplace, resulting in estimates for the thickness of the TBL that differ by up to 5 to 30 km at any given xenolith locality (*cf.* Table 1 in Priestley and McKenzie, 2006; Michaut et al., 2007). Here, we adopt the Al-in-orthopyroxene barometer of Nickel and Green (1985) and the well-calibrated enstatite-in-clinopyroxene thermometer of Nimis and Taylor (2000). For northern Lesotho, this combination yields conductive *P–T* conditions up to ~45 kbar (~170 km) and ~1050 °C. Peridotites with depleted composition (i.e., with olivine Mg# >0.92 or orthopyroxene Mg# >0.93) occur at temperatures up to ~1250 °C, but are rarely considered "lithosphere" because they frequently carry a metasomatic overprint of asthenospheric affinity (e.g., O'Reilly and Griffin, 2006). The same material is commonly thermally disturbed and should be viewed as occupying a *thermal transition layer* overlying the asthenosphere, at least for timescales equivalent to the relaxation of thermal anomalies near the base of the lithosphere (> 100 Ma; Eaton and Frederiksen, 2007).

A globally unique record of supra-adiabatic temperatures occurs in deformed xenoliths from a number of northern Lesotho kimberlites (Fig. 3). A few of these xenoliths contain fertile, pyrolite-like bulk-rock and mineral compositions (e.g., olivine with Mg# 0.89) and could represent the only known samples that approach compositional and thermal requirements for "asthenosphere" beneath cratonic lithosphere.

3.2. Northern Lesotho xenocrysts: expanding the data set

Due to their abundance in heavy-mineral concentrates, xenocrysts of garnet and clinopyroxene provide a statistically robust and efficient means to survey mantle materials entrained by kimberlites. Garnets are the minerals of choice in this application, because their major-element compositions are diagnostic of a large range of mantle rock types (e.g., Sobolev et al., 1973; Grütter et al., 2004) and single-mineral thermobarometry techniques are applicable to the Cr-pyrope varieties that occur in depleted peridotite (see O'Reilly and Griffin, 2006 for a recent summary with applications). Most public-domain garnet xenocryst data sets lack the detailed trace-element compositions required to apply Ni-

in-garnet thermometry. Hence, we use a combination of garnet major- and minor-element techniques (after Grütter et al., 1999; 2006) that permit representation of lithosphere sections in terms of temperature, mineral assemblage, garnet geochemistry and the Mg-number (or forsterite content) of mantle olivine.

Some important geochemical features of garnets in cratonic xenoliths are shown in Fig. 4. Lherzolite-hosted G9 garnets dominantly occur with FO91 to FO93 olivine, substantially more magnesian than olivine in basalt-hosted xenolith suites (FO89 to FO91) and "asthenospheric" olivine (~FO89). Low-Ca G10 garnets, long considered the uniquely distinctive index mineral of diamond-facies cratonic lithosphere (e.g., Boyd and Gurney, 1982), coexist with FO92.5 to FO95 olivine and invariably have TiO_2<0.2 wt.%. The depth distribution and relative abundance of Ti-poor and Ti-enriched Cr-pyrope garnets indicate the extent to which depleted lithospheric peridotite has been modified geochemically, a process normally observed to occur in association with dynamic recrystallisation crystallization inside the thermal transition layer.

Garnet xenocrysts from northern Lesotho kimberlites closely mirror the described xenolith suite compositionally, and expand the range to higher TiO_2, lower CaO and higher Cr_2O_3 (Fig. 5). Distinctively cratonic G10 garnets occur at P~46.7 kbar (using the minimum-pressure barometer of Grütter et al., 2006) and temperatures up to T~1190 °C (using T–Mn, an updated version of the Mn-thermometer of Grütter et al., 1999). Peridotite with Mg-rich olivine (FO>92) dominates the section at 550–1080 °C, but diminishes at higher temperatures and is effectively absent at T>1230 °C (Fig. 5). High-Ti garnet (with TiO_2>0.4 wt.%) and Fe-enriched olivine (FO89 to FO91) are significant in the section at T>880 °C and are dominant over the interval 1080 to 1230 °C.

The combined xenolith and xenocryst data set permits placement of a thermal transition layer with unquestionably relict cratonic compositions at 1080 to 1230 °C, corresponding roughly to the interval 47 to 51 kbar (180–195 km) on the disturbed northern Lesotho geotherm (arrows in Fig. 5). The entire mantle section at higher temperature and pressure is apparently occupied by "asthenosphere-like" melt-metasomatised peridotite with dynamically recrystallized textures. The preservation of highly depleted Os characteristics and Archean Re-depletion model ages in these modified rock types indicates billion-year stability, most likely as part of a cratonic root (e.g., Pearson et al., 1995).

3.3. Kimberley: a conductive mantle section

The peridotite xenolith suite from the mine dumps at Kimberley, South Africa, contains abundant coarse-textured garnet lherzolites with conductive thermobarometry results (Boyd and Nixon, 1978). Deformed high-temperature peridotite xenoliths are effectively absent and there is negligible evidence for Ti- or Fe-enrichment at depth (Fig. 6). Olivine compositions fall dominantly in the range FO91 to FO93.5 throughout the entire section, a trait that matches olivine compositions inverted from garnet xenocryst data. G10 garnets are most common in the lower half of the section, occur across diamond-facies conditions up to the limit of the section at T~1250 °C, and indicate 51 kbar (~195 km) as a minimum depth for the depleted lithosphere. The available data do not support delineation of a thermal boundary layer. Differential sampling patterns indicate a subtle minimum at T~1100 °C, suggesting that kimberlite magmas may have encountered a mechanical boundary at P~48 kbar, corresponding to the base of the known conductive geotherm for Kimberley (Fig. 6). The Frank Smith kimberlite is well known to host deformed high-temperature peridotites with Mg-rich olivine and Cr-pyrope garnets zoned toward Fe- and Ti-enriched compositions (Smith and Boyd, 1989; Fig. 6). These rocks provide confirmation of a depleted mantle underlying the Kimberley area to pressures of at least 56 kbar (~215 km), prior to transient thermal disturbances. There is no evidence of "asthenospheric" materials in the data set.

3.4. Central Slave: a layered lithosphere

Griffin et al. (1999) characterised the cratonic mantle underlying the Lac de Gras kimberlites in the central Slave craton, Canada, as compositionally layered and having a stepped geotherm. Our xenocryst data (Fig. 7) show G10 garnets and FO93 olivine dominating the section at low (graphite-facies) temperatures, and declining in relative abundance to the limit of the section at pressures close to 60 kbar (~230 km) and T~1300 °C. Garnet lherzolite xenoliths and G9 garnet xenocrysts are dominant at T>750 °C and are correlated with a subtle TiO_2 increase with depth and a steady decrease in average FO from 92.3 at 700 °C to 91.3 at 1200 °C. The entire section is depleted relative to "asthenosphere" and unusually low trace-element contents of Y, Ga, Ti and Zr in garnet aid in defining an ultra-depleted layer at T<900 °C (Griffin et al., 1999).

Our xenolith thermobarometry results generally concur with those of Griffin et al. (1999) in showing a 35 mW/m^2 model conductive geotherm for the ultra-depleted layer, with an apparent increase to a 40 mW/m^2 model to depth (Fig. 7). The "stepped geotherm" thus defined is not related to visible Fe–Ti-metasomatism, nor necessarily to dynamically deformed xenolith textures as would typically occur in most other cratonic settings. In this case the thermal structure of the deep lithosphere appears largely unrelated to the compositional structure, at least for the 16 Ma timescale in the Eocene over which kimberlite magmas sampled the central Slave craton mantle (Creaser et al., 2004). We tentatively interpret the shallowest limit for a

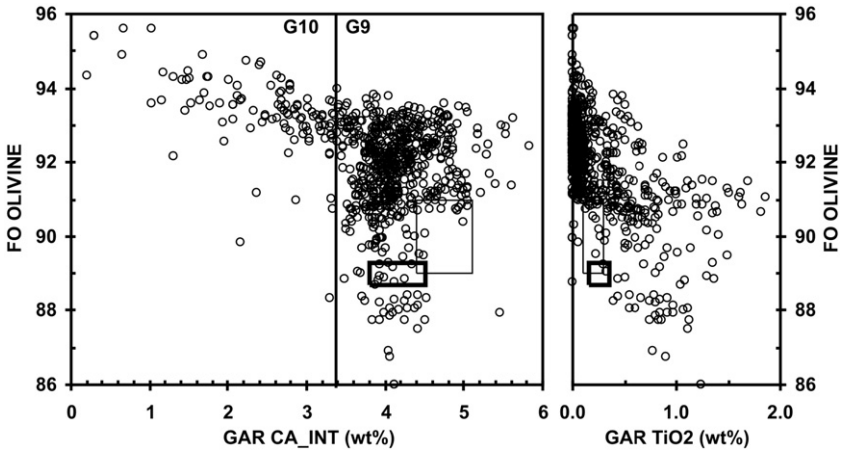

Fig. 4. Summary diagrams outlining important compositional characteristics of garnet and olivine in cratonic peridotite xenoliths from South Africa (n=648) and Lesotho (n=240). The cratonic data show little compositional overlap with peridotite xenoliths hosted by alkali basalts in non-cratonic settings (light rectangles), nor with pyrolite-model compositions expected for asthenosphere (bold rectangles). The garnet calcium-intercept projection (CA_INT) and G10/G9 classification is from Grütter et al. (2004). Xenolith data sources as in Grütter and Moore (2003).

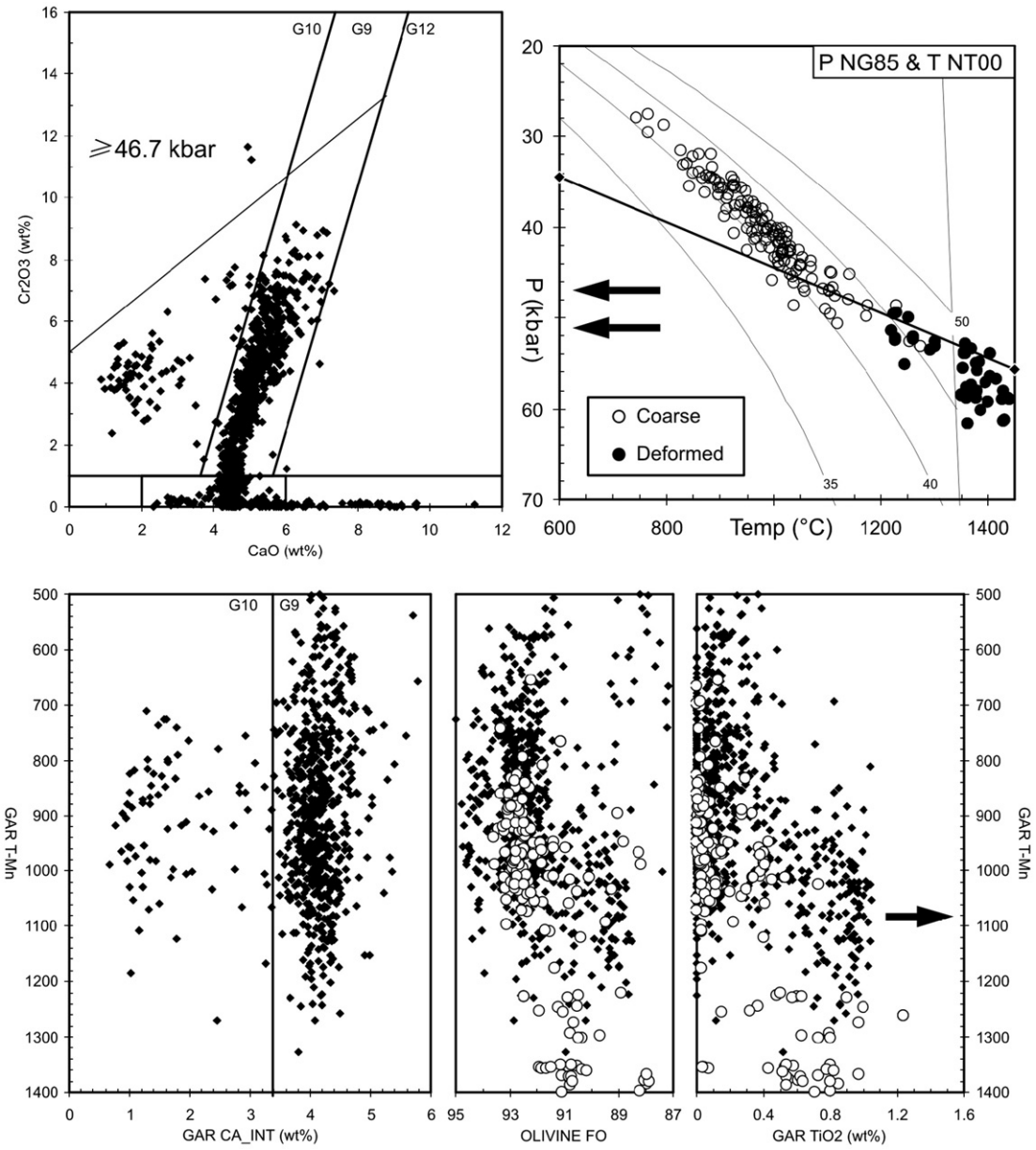

Fig. 5. Composition, pressure and temperature relations for garnet xenocrysts (solid diamonds) and garnet lherzolite xenoliths (circles) from northern Lesotho (Kaapvaal craton). The three lower panels show temperature-indexed compositional parameters (as in Fig. 3) that permit "depth" estimates to be made for depleted peridotite residing within a thermal boundary layer (arrows). Mn-in-garnet temperatures (GAR T-Mn) and olivine FO calculations for xenocrysts are modified after Grütter et al. (1999). Compositional boundaries marked on the Cr_2O_3 versus CaO diagram are discussed in Grütter et al. (2004). High-Cr_2O_3 G10 garnets are labelled with a minimum pressure (as formulated by Grütter et al., 2006). Xenolith data sources as in Grütter and Moore (2003); xenocryst data from six open-file reports published by the Council for Geoscience, South Africa (D. de Bruin, pers. comm., May 2007).

thermal boundary layer to be at $P \sim 45$ kbar or $P \sim 56$ kbar (~170–215 km; Fig. 7). Despite this uncertainty, we are able to show that depleted peridotite exists throughout the section to the deepest levels represented, with no trace of FO89 "asthenospheric" olivine compositions even at temperatures close to the adiabat (Fig. 7).

3.5. Finland: a craton-margin setting

Kimberlites in the Fennoscandian Shield of eastern Finland have sampled the lithosphere within 10 s of kilometres of the boundary of the Archean Karelian craton with the Proterozoic Svecofennian belt. The peridotitic mantle in this setting is strongly dominated by G9 (lherzolitic) garnets, and calcic varieties apparently occur at $T < 800$ °C (Fig. 8). Rare G10 garnets occur through the section and provide a minimum pressure of 52 kbar (~200 km) for depleted peridotite. Lherzolitic olivine maintains depleted FO91 to FO93 compositions over the whole temperature range, up to the maximum of 1320 °C. Our xenocryst data record significant Fe- and Ti-enrichment in the range 850–1320 °C, and low-Ti peridotite is uncommon at $T > 1060$ °C (Fig. 8). We place the top of a thermal transition layer at this temperature and allow it to extend downward to $T \sim 1300$ °C. The corresponding pressures are difficult to assign because available xenolith thermobarometry results are scattered at depth, possibly a result of thermal disturbance.

Apart from the low overall abundance of G10 garnets and existence of an ultra-depleted harzburgitic layer (Lehtonen et al., 2004), previously thought to be unique to the Slave craton (Griffin et al., 1999), the overall features of the Finnish lithosphere are intrinsically no different from that observed underlying other cratonic core regions. Specifically, no "asthenophere" is apparent in a mantle section that extends to near-

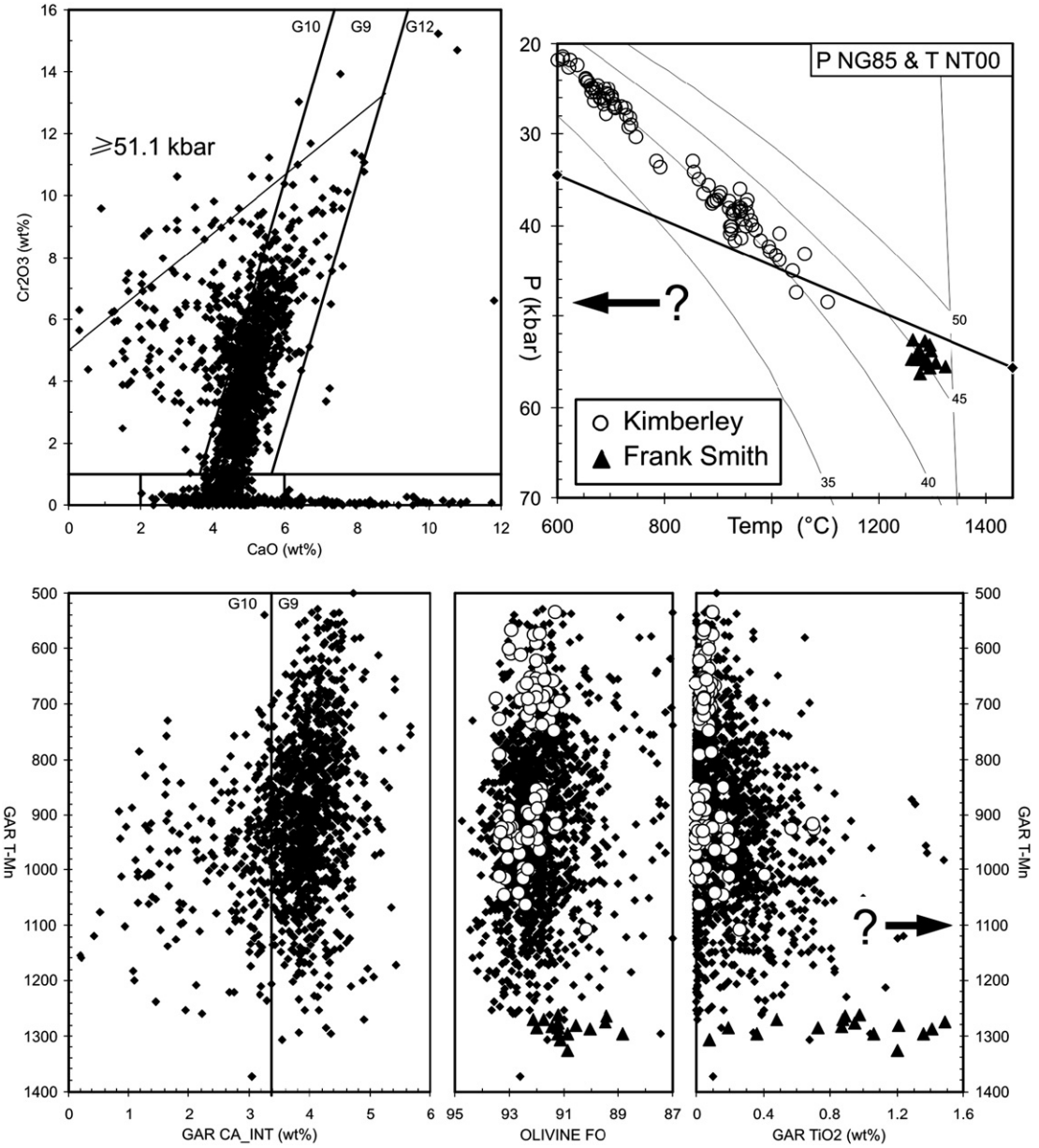

Fig. 6. Composition, pressure and temperature relations for garnet xenocrysts (solid diamonds) from the Kimberley area and garnet lherzolite xenoliths (circles) from the Kimberley mine dumps (Kaapvaal craton). Triangles denote deformed high-temperature xenoliths with compositionally zoned garnets from Frank Smith. Arrows denote an inferred mechanical boundary at $T \sim 1100$ °C and $P \sim 48$ kbar. Xenolith data sources as in Grütter and Moore (2003); xenocryst data as in Grütter et al. (2006) and derived from five additional open-file reports published by the Council for Geoscience, South Africa (D. de Bruin, pers. comm., May 2007).

adiabatic temperatures at some of the highest pressures known for any kimberlite-borne xenolith suite (~65 kbar, ~245 km; Fig. 8).

4. The rheological lithosphere

4.1. Deformation mechanisms and seismic anisotropy

The differential motion between tectonic plates and the asthenosphere is accommodated at the LAB by one of two primary creep mechanisms (Karato and Wu, 1993). Laboratory studies show that at small grain size, low stress level, or both, subsolidus deformation occurs through diffusive mass transport at the molecular level between grain boundaries (*diffusion creep*). Conversely, at large grain size, high stress level or both, subsolidus deformation occurs through the motion of crystalline dislocations within grains (*dislocation creep*). Under any given set of conditions (temperature, pressure, grain size, stress and water content) the dominant mechanism is the one that produces the highest strain rate, or equivalently

Table 1
Flow law parameters for olivine (from Korenaga and Karato, 2008)

Mechanism/parameter	Dry	Wet
Dislocation creep		
A (s^{-1})	2.05×10^{30}	9.31×10^{29}
n	4.94	3.6
m	0	0
r	0	1.95
E (kJ mol^{-1})	610	523
V (cm^3 mol^{-1})	13.4	4.23
Diffusion creep		
A (s^{-1})	9.84×10^{19}	1.81×10^{29}
n	1.0	1.0
m	2.98	2.56
r	0	1.93
E (kJ mol^{-1})	261	387
V (cm^3 mol^{-1})	5.9	25.2

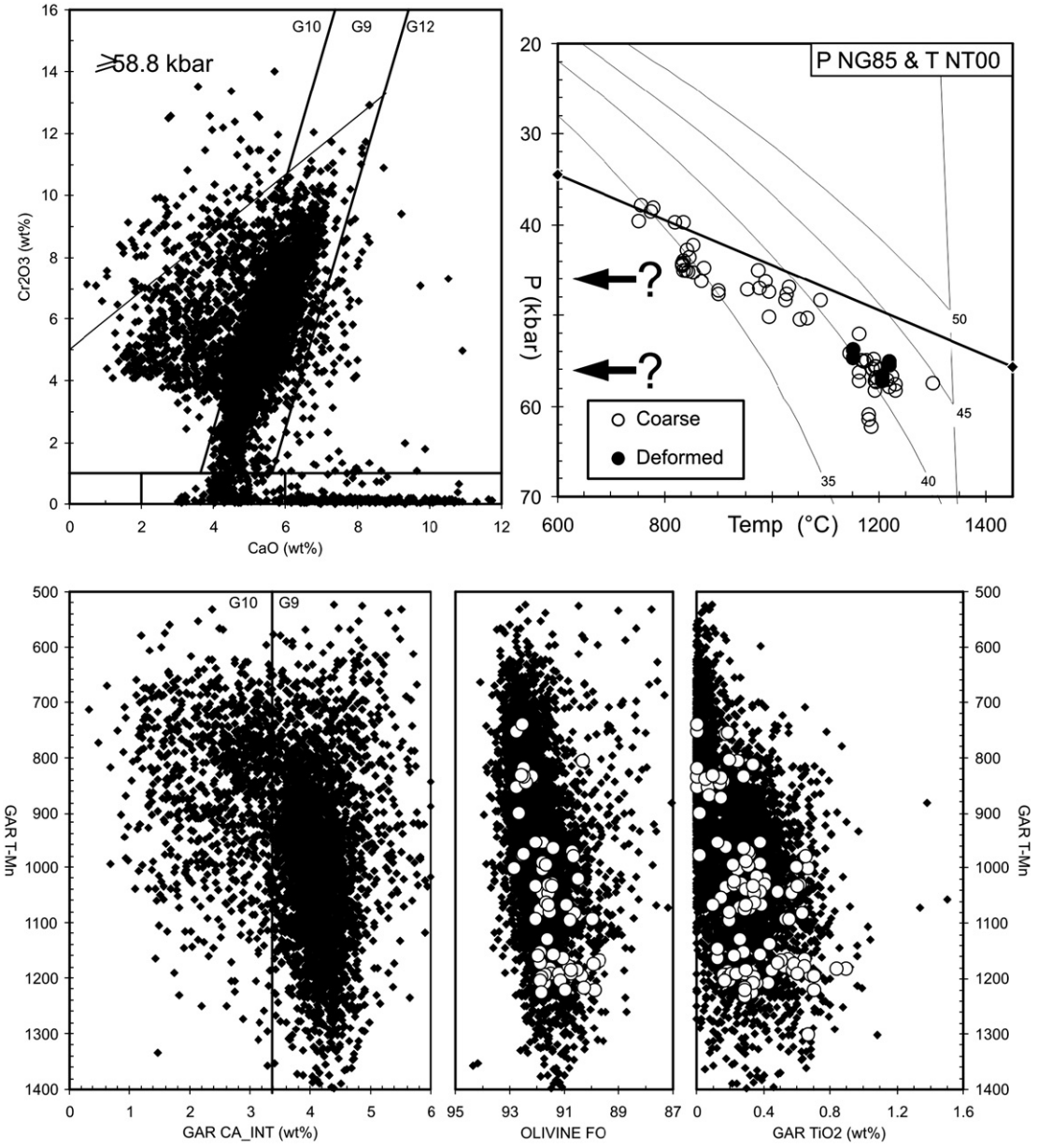

Fig. 7. Composition, pressure and temperature relations for garnet xenocrysts from the Lac de Gras mine leases (solid diamonds) and garnet lherzolite xenoliths from economic kimberlites (circles) at the Ekati and Diavik mines (Slave craton). Arrows denote two possible choices for the shallow limit of a thermal transition layer. Xenolith data sources as in Grütter and Moore (2003); xenocryst data from Armstrong (2001).

the least amount of work to produce a given level of strain. The upper mantle may thus be partitioned into regions where either diffusion creep or dislocation creep dominates. The boundary between these regions may change with time, since at high strain rates dynamic recrystallization may lead to grain-size reduction that will tend to favour diffusion creep. These two mechanisms have significantly different consequences for the development of detectable strain fabrics; dislocation creep results in the development of lattice–preferred orientation (LPO) of mantle minerals that may be detectable using seismic or magnetotelluric methods, whereas diffusion creep does not (Karato and Wu, 1993).

The flow laws that govern rheological behaviour of polycrystalline mantle rocks are poorly known. To simplify the analysis, it is commonly assumed that mantle deformation is controlled by the rheological properties of olivine, since this is the most abundant mineral in the upper mantle as well as the weakest component under a wide range of conditions (e.g., Durham and Goetze, 1977; Ceuleneer et al., 1988; Mackwell, 1991). For olivine aggregates under steady-state conditions, the strain rate $\dot{\varepsilon}$ for each creep mechanism may be expressed in power-law form as a function of temperature (T), pressure (P), grain size (d), water content (C_{OH}) and shear stress (σ):

$$\dot{\epsilon} = A\left(\frac{\sigma}{\mu}\right)^{n}\left(\frac{d}{b}\right)^{-m} C_{OH}^{r} e^{\frac{-(E+PV)}{RT}}. \quad (1)$$

The flow-law parameters in this expression are: A, the preexponential factor; E, the activation energy; V, the activation volume, and m, n and r, exponents for grain size, stress and water content, respectively. In addition, μ=80 GPa is the reference shear modulus, b=0.5 nm is the length of the Burgers vector and R is the gas constant. Each of the flow-law parameters takes on different values, depending on creep mechanism (diffusion or dislocation) and whether ambient conditions are wet or dry. Here, we use parameter values reported by Korenaga and Karato (2008) based on a Bayesian analysis of experimental data that considers inter-run bias and experimental uncertainties (Table 1). For many of the parameters, their results confirm parameter values from previous compilations (Karato and Wu, 1993; Hirth and Kohlstedt, 2003); however,

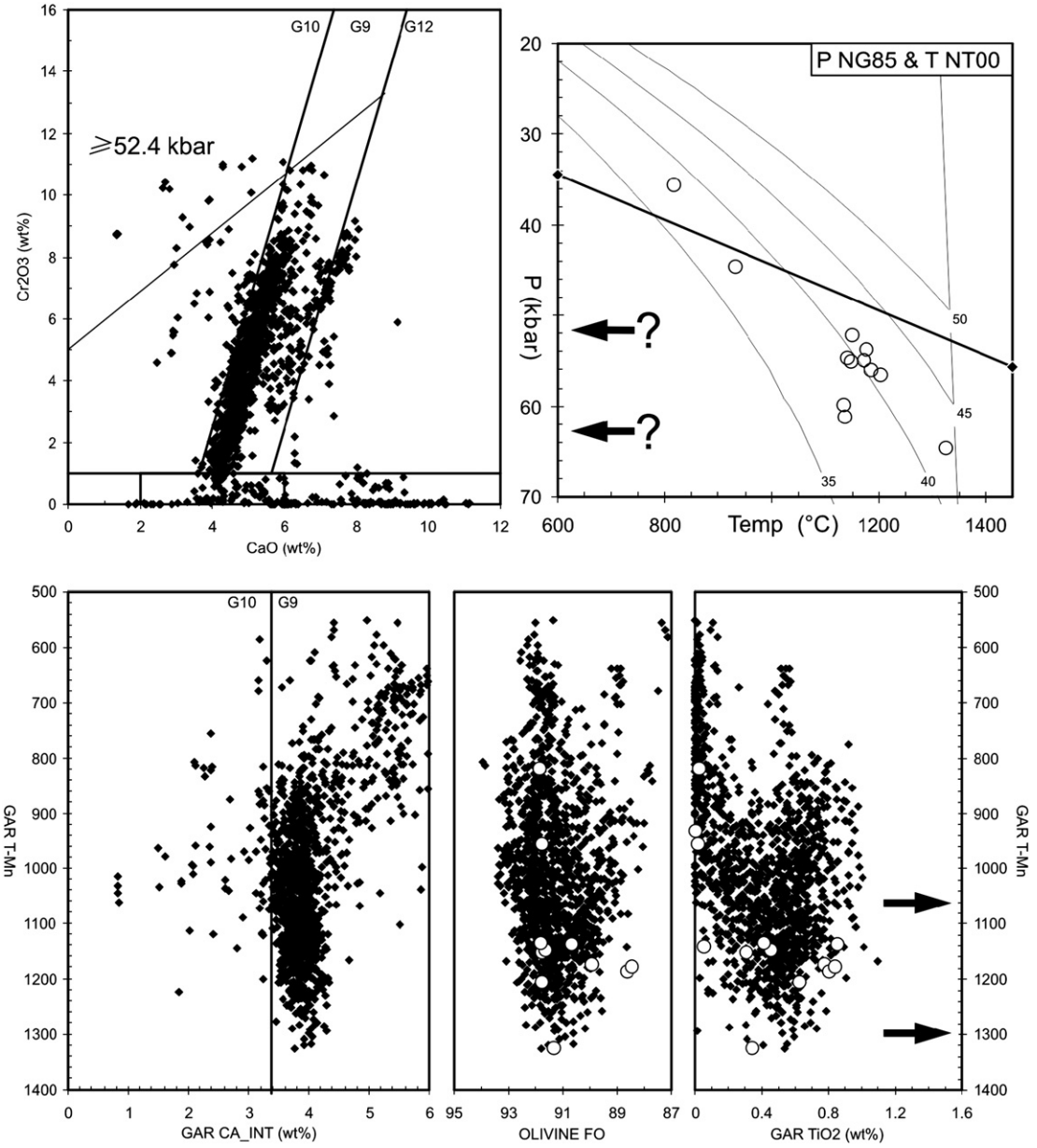

Fig. 8. Composition, pressure and temperature relations for garnet lherzolite xenoliths (circles) and garnet xenocrysts (solid diamonds) from the Kuopio-Kaavi kimberlites and till samples in the surrounding area (Fennoscandia). Arrows in the lower panels denote the limits of depleted peridotite residing within a thermal transition layer; their corresponding pressures in the upper panel are poorly resolved with the available xenolith thermobarometry results. Xenolith data from Kukkonen and Peltonen (1999); xenocryst data subsetted from Lehtonen et al. (2005a, 2005b).

their value for the stress exponent of dislocation creep is significantly higher than past studies (~5 rather than ~3.5). As elaborated below, this has the effect of broadening the region where dislocation creep is the dominant mechanism.

4.2. Creep modeling

To model the rheology and shear stress within the lithosphere, we have applied the constraint that the integrated strain rate of the upper mantle should match the velocity difference (Δv) between the surface and the underlying mantle,

$$\int_{z_0}^{0} \dot{\epsilon}\, dz = \Delta v, \tag{2}$$

where z denotes depth measured from the surface and z_0 is taken to be sufficiently far beneath the LAB that the mantle can be assumed to be moving independently of the plate. In our calculations below, we use z_0 = 600 km. In addition, Δv is taken as the difference in horizontal velocity between the plate motion defined by HS3-NUVEL1A (Gripp and Gordon, 2002) and a flow model at 250 km computed by Behn et al. (2004). The flow calculations for the latter model are driven entirely by mantle density variations inferred from seismic tomography and provide an independent reference velocity field for estimating Δv. Following Bokelmann and Silver (2002), we assume a constant stress level below the Moho. For strain rate given by

$$\dot{\epsilon} = \max\left(\dot{\epsilon}_{dis,dry}, \dot{\epsilon}_{dis,wet}\right) + \max\left(\dot{\epsilon}_{dif,dry}, \dot{\epsilon}_{dif,wet}\right), \tag{3}$$

we solve for the level of shear stress σ that satisfies Eq. (2), where the subscripts in Eq. (3) indicate the creep mode and presence (or absence) of water.

Fig. 9 presents results of creep calculations under dry conditions (typical water contents in the continental mantle are thought to be less than ~500 ppm; Bell and Rossman, 1992) using a uniform grain

size of 1 cm, consistent with the coarse grain size observed in cratonic mantle xenolith samples. We estimate the following differential velocities for xenolith localities in the three cratons: 5.8 mm/yr (Kaapvaal), 18.4 mm/yr (Slave) and 20.8 mm/yr (Fennoscandia). To obtain a temperature profile, we used published geotherms for the Kaapvaal craton from Jones (1988), the Slave craton (for the case q_m= 18.2 mW/m^2) by Russell et al. (2001), and Fennoscandia by Kukkonen and Peltonen (1999). We remark that these steady-state models may slightly underestimate the geotherm, due to transient thermal effects (Michaut et al., 2007). Our results suggest that, under dry conditions, dislocation creep is the dominant deformation mechanism in the asthenosphere and the lowermost 60–70 km of the lithosphere. The dominance of dislocation creep in these depth ranges implies that strain fabrics arising from LPO of olivine should be produced, which may be detectable using seismic data. Due to the very low strain rate within the lithospheric mantle, any antecedant strain fabrics at shallower depth levels would be preserved, leading in some cases to two-layer anisotropy (e.g., Snyder and Bruneton, 2007).

The shear stress required to fit the differential velocity data for each craton lies within a very narrow range from 2.15 Mpa to 2.73 MPa, well within previous estimates (e.g., Bokelmann and Silver, 2002; Conrad and Lithgow-Bertelloni, 2006). This relatively narrow range of stress values for the various regions exists, despite large differences in differential velocity in the three cases, due to the large value of the stress exponent for dislocation creep used here and obtained by Korenaga and Karato (2008). The minimum of effective viscosity obtained using this approach is ~10^{20} Pa s, which is close to the minimum viscosity for the upper mantle found by Forte and Mitrovica (1996) based on joint inversion of long-wavelength convection and post-glacial rebound data.

As a working definition, we propose a strain rate of 10^{-15} s^{-1} to approximate the top of the LAB. Under dry conditions, this yields depth estimates of 220–245 km (Fig. 9), generally consistent with independent constraints from xenolith studies (Table 2). Although this choice of strain rate is somewhat arbitrary, increasing it by an order of magnitude or more has negligible effect on the inferred depth of the LAB. This working definition places the LAB slightly shallower than the depth at which the geotherm intersects the adiabat.

Based on inversion of magnetotelluric data, Hirth et al. (2000) proposed that the mantle in the depth range of ~250–400 km beneath both ocean basins and cratons has similar water content, whereas cratonic lithosphere at shallower depths is significantly "drier" than the global average. They suggested that this difference in water content may contribute significantly to the high strength of cratonic lithosphere relative to other parts of the mantle. To explore the influence of water on the rheological properties of the LAB, we have performed flow calculations for the Slave craton, similar to those above but using various values of mantle water content (C_{OH}). One series of models uses a uniform level of C_{OH} in the mantle, with levels of 0, 10 and 100 ppm by weight. Another model, based on Hirth et al. (2000), uses a value of zero in the lithosphere and 200 ppm below the LAB, which is assumed to be at 250 km depth.

Our modelling results (Fig. 10) show that the addition of even a small amount of water to the mantle reduces the effective viscosity and hence the level of stress required to fit the differential velocity boundary condition. As noted above, in the case of a completely dry mantle a zone of high strain rate, associated with mechanical decoupling between the lithosphere and asthenosphere, is thermally controlled and localized near the LAB. With even a small amount of water this zone of mechanical decoupling has a step-like character

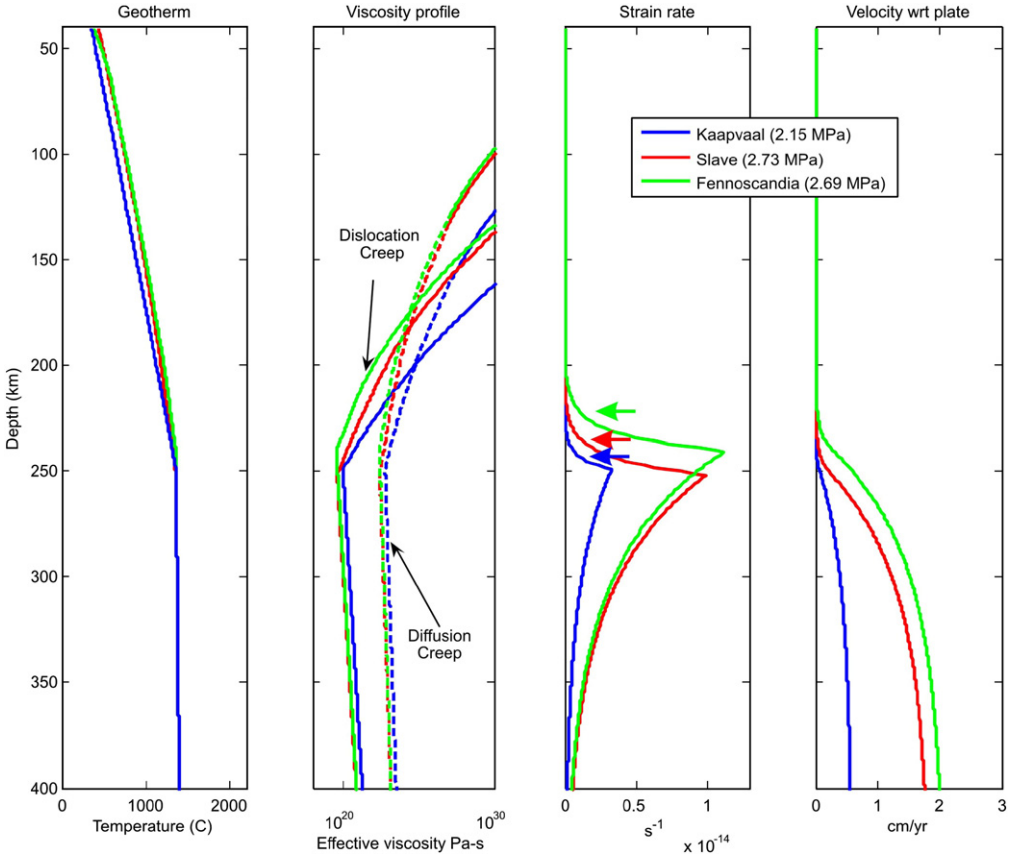

Fig. 9. Geotherm, effective viscosity, strain rate and differential velocity profiles computed by solving Eqs. (1)–(3) assuming a dry rheology and a constant mantle stress level indicated in the legend. Grain size is assumed to be constant (1 cm). Flow parameters are from Korenaga and Karato (2008) and listed in Table 1. The lithosphere–asthenosphere boundary (LAB) is indicated by bold arrows and coincides with the depth where the strain rate is 10^{-15} s^{-1}, between 220 and 245 km (Table 2). Dislocation creep is the dominant deformation mechanism in the lower lithosphere and asthenosphere, which should result in detectable LPO fabrics.

and is distributed more broadly within the asthenosphere. If the lithosphere is dry and the asthenosphere is wet, as in model HEC, the depth of the LAB is entirely controlled by the distribution of water in the mantle. In this case, the LAB and base of the TBL do not necessarily coincide.

The transition from diffusion creep to dislocation creep occurs about 60–70 km shallower than the LAB in every model except model HEC, where it coincides precisely with the LAB. We remark that some previous studies of mantle creep (e.g., Bokelmann and Silver, 2002) infer a deeper downward transition back to diffusion-dominated creep. In our models, this transition is absent and the lower lithosphere and asthenosphere are located entirely within the dislocation creep regime, implying a relatively thick region within which anisotropy from viscous drag due to plate motion may develop. This difference arises from several factors. First, the stress exponent for dislocation creep used here (from Korenaga and Karato, 2008) is significantly higher than previous estimates. In addition, we assume a grain size (1 cm) that is appropriate for coarse-textured lithospheric mantle, but somewhat larger than in most previous studies. For reasons outlined above, this larger grain size tends to favour dislocation creep over diffusion creep.

5. The seismological lithosphere

5.1. Surface-wave methods

While the *seismological lithosphere* beneath cratonic regions is commonly characterised as a lid of anomalously high shear-wave velocity from the Moho to ~100–300 km depth, its base is difficult to identify using surface waves, due to the integrating properties of the technique. Although surface waves have good sensitivity to absolute seismic velocity over a given depth range, related to the sensitivity kernels of the phases at different periods, they are relatively insensitive to the nature of the boundaries between high and low velocities. Thus a sharp velocity contrast at the base of the seismological lithosphere is generally indistinguishable from a gradual velocity gradient (Fig. 11). As discussed below, joint interpretation of surface-wave models with *S*-receiver functions offers a potential means to resolve this ambiguity, at least in principle.

Early models of the continental cratonic lithosphere (e.g., Brune and Dorman, 1963) generally showed a distinct high-velocity "lid" overlying a zone of lowered velocity. However, the sharp base was most likely an artifact of the necessarily-simple layered model parameterization, as opposed to a true reflection of seismic seismic-velocity structure or surface surface-wave resolution. In the following sections, we give a brief overview of the definitions of the cratonic lithosphere and its base from recent publications based on surface-wave studies, using both seismic-velocity variation and depth-dependent anisotropy.

5.1.1. Defining the LAB using surface-wave observations

The base of the lithosphere, or the apparent absence of an identifiable base, has been defined in several different ways through the modelling of seismic-velocity profiles from surface surface-wave data. The presence of a low-velocity zone beneath the high-velocity lid can be taken as an indication of the LAB (e.g., Bruneton et al., 2004a; Pontevivo and Thybo, 2006), though the depth range of the boundary region will depend on the model parameterization. Proxies for the LAB are given by many authors, based on a number of different criteria that stem from surface-wave observations:

- the depth range of the strongest negative velocity gradient at the base of the high-velocity mantle lid (e.g., Debayle and Kennett, 2000a; Li et al., 2003; Priestley and Debayle, 2003) or the depth to the centre of this gradient (Weeraratne et al., 2003);

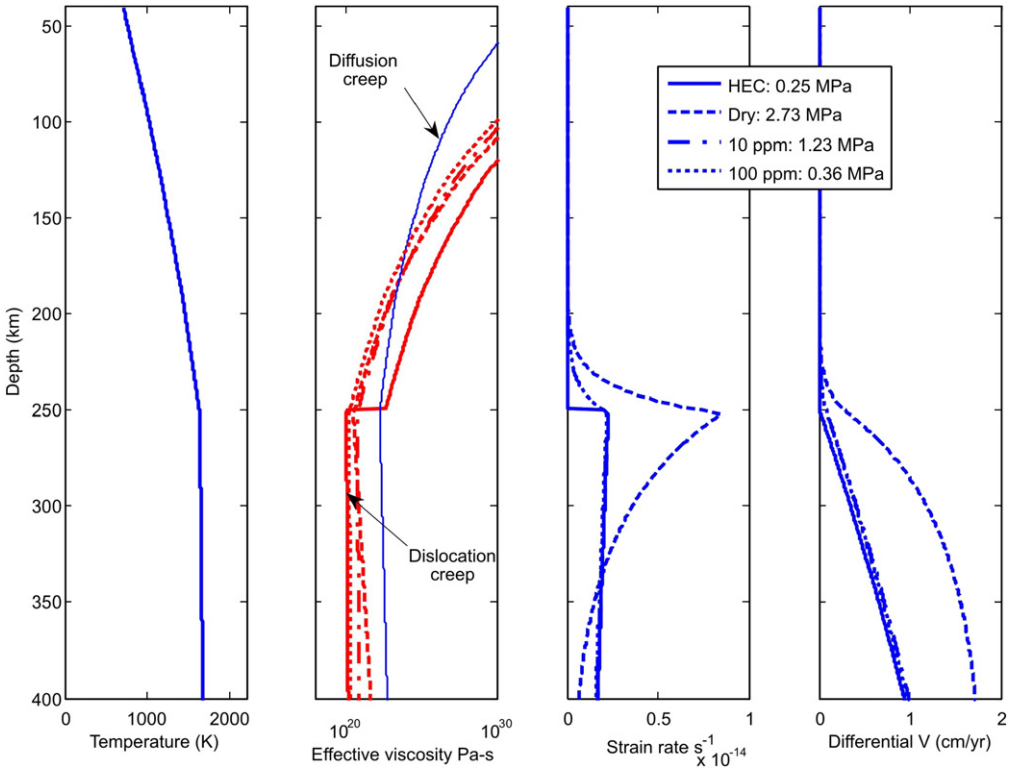

Fig. 10. Geotherm, effective viscosity, strain rate and differential velocity profiles for the Slave craton, assuming a constant mantle stress level and various values of water content (C_{OH}, ppm) expressed as a weight fraction. Grain size is assumed to be constant (1 cm). Flow parameters are from Korenaga and Karato (2008) and listed in Table 1. HEC refers to Hirth et al. (2000) and represents a model that is dry in the lithosphere, with 200 ppm C_{OH} in the asthenosphere. For model HEC, the lithosphere is a rigid layer above a thick deforming asthenosphere; for all other models, some lithospheric deformation occurs near the LAB. The dry model exhibits the thinnest zone of deformation that accommodates the differential motion between the plate and underlying mantle.

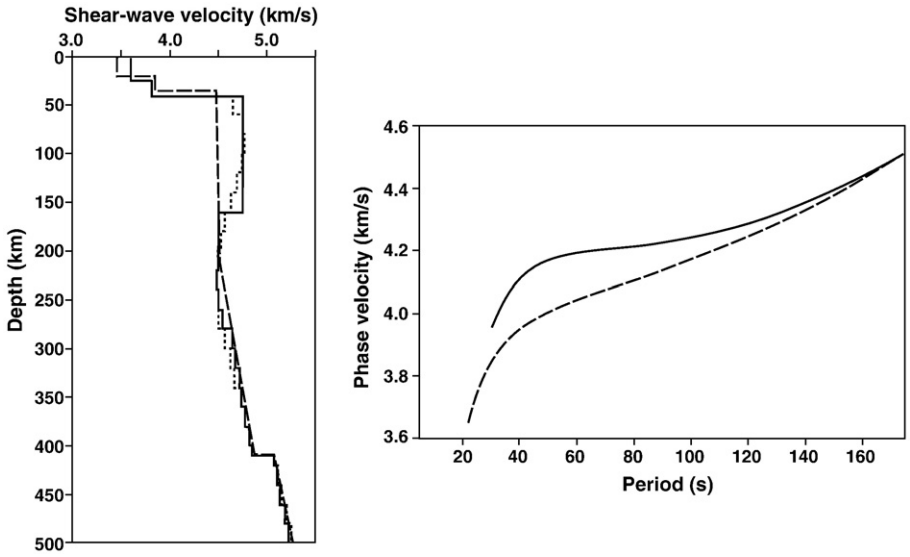

Fig. 11. Illustration of the difficulty in defining the lithosphere–asthenosphere boundary (LAB) using surface-wave dispersion analysis. The solid velocity model represents a synthetic craton model with a sharp LAB. A synthetic dispersion curve (right panel) for the fundamental-mode Rayleigh wave was calculated from this model, then inverted using a smooth starting model. The resulting velocity model and corresponding synthetic dispersion curve are shown as a dotted line. The dispersion curves for the two models are almost identical. Dashed line: AK135 global reference model.

- statistical analysis of negative velocity gradients in multiple 1-D models (Cotte et al., 2002);
- a certain contour – typically 1–2% – of positive velocity anomaly above a global reference model (e.g., Frederiksen et al., 2001; Simons and van der Hilst, 2002; Gung et al., 2003; Darbyshire et al., 2007);
- absolute velocity variation with depth — taking a specific V_s value instead of a percent velocity anomaly as a proxy (Li and Burke, 2006);
- changes in the nature of the lateral velocity heterogeneity across an array confined to a shield region (Bruneton et al., 2004b);
- changes in orientation and/or intensity of seismic anisotropy (e.g. Gaherty and Jordan, 1995).

The consistency of these proxy measurements may vary from study to study. In many cases, it is simply not possible to compare the differing definitions for the LAB due to the nature of the velocity models. For example, a model may show no appreciable negative velocity gradient, but still converge with the global reference models at depth. Even in the cases where a strong negative velocity gradient appears beneath the lithospheric lid, an uncertainty of several tens of kilometres in the position of the LAB should be noted. In several cases, the depth of the LAB is quoted without reference to specific criteria for the definition of the lithosphere base (e.g., Ritsema and van Heijst, 2000; Chevrot and Zhao, 2007), and the reader must inspect the velocity models carefully in order to make any meaningful comparison of the results presented with those from other surface-wave models of the region.

5.1.2. Azimuthal anisotropy

Azimuthal anisotropy is a class of seismic anisotropy associated with mantle fabrics produced by horizontal shear with a preferred orientation. Surface-wave techniques are extremely valuable in studies of anisotropy as they are able to provide information on the depth-dependence of these anisotropic fabrics in the upper mantle (Plomerova et al., 2002), unlike most body-wave studies such as SKS splitting analysis (e.g., Fouch and Rondenay, 2006 and references therein). A number of Rayleigh-wave studies, using either waveform inversion of regional earthquakes or phase velocity measurements of teleseismic earthquakes across an array, solve both for shear-velocity heterogeneity and azimuthal anisotropy. The changes with depth in the amplitude, lateral smoothness or predominant direction of the azimuthal anisotropy can be interpreted in terms of the evolution from frozen lithospheric anisotropy to alignments resulting from viscous coupling to the sublithospheric mantle (e.g., Debayle and Kennett, 2000a; Plomerova et al., 2002); Debayle et al., 2005; Sebai et al., 2006). For example, Sebai et al. (2006) report a significant change in the properties of azimuthal anisotropy beneath the southern African cratons at ~180 km depth and interpret this transition as the LAB. This change in anisotropy occurs within the depth range of anomalously high shear-wave velocity, traditionally regarded by seismologists as indicative of lithospheric mantle.

5.1.3. Radial anisotropy

Radial anisotropy is a class of seismic anisotropy related to mantle fabrics produced by horizontal shear, with no apparent preferred orientation. The lack of a preferred fast direction may be caused by long-wavelength averaging of randomly oriented, azimuthally anisotropic domains in the continental lithosphere (Gaherty and Jordan, 1995). Alternatively, radial anisotropy may represent weak azimuthal anisotropy within an orthorhombic symmetry system (e.g., Babuška and Plomerová, 2006).

Radial anisotropy may be resolved in surface-wave studies by examining the discrepancy between Rayleigh and Love wave dispersion properties, which are sensitive to the velocities of vertically (SV) and horizontally (SH) polarized shear waves, respectively. Gung et al. (2003) examined global tomographic models based on V_{SV} and V_{SH}, and concluded that significant radial anisotropy is present under most cratons in the ~250–400 km depth range, with $V_{SH} > V_{SV}$. The presence of this anisotropy is attributed to flow-induced shear in the asthenosphere, although Gaherty and Jordan (1995) and Gaherty et al. (1999) argue that beneath the Australian craton radial anisotropy is confined to the lithosphere. A number of regional- and continental-scale surface-wave studies have examined variations in radial anisotropy (e.g., Debayle and Kennett, 2000b; Saltzer, 2002; Gaherty, 2004; Pedersen et al., 2006; Sebai et al., 2006), though many of these studies lack sufficient simultaneous depth resolution of Love and Rayleigh waves to identify the base of the region of radial anisotropy. The radial anisotropy modelled for the southern African cratons by Sebai et al. (2006) decreases gradually with increasing depth down to ~300 km.

5.1.4. Surface waves and SKS splitting

Many authors have attempted to use a correspondence between surface-wave anisotropy and SKS splitting analyses to interpret the anisotropic structure of the cratonic lithosphere and the asthenosphere beneath. In SKS splitting interpretations, back-azimuthal variation of delay time and fast direction are used to infer the presence of single or multiple anisotropic layers in the mantle, but depth is poorly resolved. Typically, the most that can be confidently interpreted is the relative depth (upper versus lower layer) of two-layered anisotropic fabric, and inferences of maximum and minimum layer thicknesses based on integration of delay time information. In regions that are well-covered by seismograph stations, lateral resolution of changes in anisotropic structure is good, and Fresnel zone-based arguments can be used to constrain depth extent of anisotropy (e.g., Rümpker and Ryberg, 2000).

In contrast, surface waves provide good depth resolution but relatively poorer lateral resolution. While a full joint interpretation of anisotropy using SKS splitting and surface waves (e.g., Snyder and Bruneton, 2007) is relatively rare, many authors have made comparisons of the results from the two techniques (Debayle and Kennett, 2000a; Li et al., 2003; Gaherty, 2004). Positive correlations are used to constrain the depth range of anisotropy inferred from SKS splits (e.g., Snyder and Bruneton, 2007), whereas negative results may be used to infer that the SKS anisotropy originates from a region deeper than the resolution extent of the surface-wave study (Li et al., 2003). Alternatively, discrepancies between surface-wave and SKS-based interpretations may be interpreted as arising from complex and rapidly-varying patterns of anisotropy, for which the net effects may be seen quite differently when sampled with surface or body waves (e.g., Saltzer, 2002; Simons et al., 2002; Li et al., 2003; Gaherty, 2004; Pedersen et al., 2006).

5.1.5. Mapping the LAB using S-receiver functions

Receiver functions (Langston 1977; Vinnik 1977) are routinely used to detect seismic discontinuities in the crust and upper mantle. Conventional (*P*-) receiver functions are based on isolation of *P*-to-*S* converted waves, generated at seismic discontinuities, from the *P*-wave *coda*. Although there have been some successful applications of *P* receiver functions for observation of the LAB (Rychert et al., 2005; Chen et al., 2006), this method is generally of limited value for detecting interfaces in the mantle lithosphere, due to interference of primary conversions with strong crustal reverberations. A recent technique employing *S*-to-*P* conversions, the *S*-receiver function (SRF; Yuan et al., 2006), appears promising for detecting the LAB beneath seismic stations.

There are a number of technical challenges specific to *S*–*P* conversions compared to *P*–*S* conversions (Yuan et al., 2006). *S* waves are generally characterised by lower frequencies than *P* waves, resulting in a lower spatial resolution. Most previous studies thus focused on identification of *S*-to-*P* converted waves from long-period seismograms. To avoid post-critical incidence, *S*-to-*P* converted waves can only be observed over a limited teleseismic distance range (Yuan et al., 2006). Since *S* waves are not first arrivals within this distance range, they typically arrive within the *P*-wave coda and interfere with other phases. Painstaking polarity analysis to distinguish the *S*-to-*P* converted waves from *S* waves has been used to identify the LAB (Sacks and Snoke 1977; Sacks et al., 1979; Snoke et al., 1977; Bock and Kind 1991).

Farra and Vinnik (2000) were the first to propose the application of receiver-function analysis as a way to isolate *S*-to-*P* converted phases from the incident *S* waves. The method has since been improved by introducing stacks of individual *S*-receiver functions according to the geographic locations of piercing points, and used to map the LAB in various tectonic settings (e.g., Li et al., 2004; Kumar et al., 2005; 2006; Sodoudi et al., 2006). Like conventional receiver functions, *S*-receiver functions use a deconvolution process to remove source and path effects in order to isolate receiver-side Earth response based on seismic mode conversions. Whereas conventional receiver functions use the teleseismic *P* wave (measured on one component, such as the vertical component) to extract *P*–*S* converted phases, *S*-receiver functions use the teleseismic *S* wave to extract *S*–*P* converted phases. An important practical difference is that *P*–*S* phases arrive after the *P* wave in the case of conventional receiver functions, whereas *S*–*P* phases are precursors to *S*. As a result, SRFs are less affected by crustal reverberations that tend to obscure the LAB on conventional receiver functions. Since SRFs are computed as a function of traveltime, independent knowledge of *P*- and *S*-wave velocities is required to convert the observations to depth.

In Fig. 12, we compare synthetic *P* and *S*-receiver functions for 3 models with different LAB sharpness (Fig. 12A). Synthetic receiver functions (Fig. 12B) are calculated by a Haskell matrix propagation approach with an assumption of plane-wave incidence. The dominant wave periods of the *P* and *S*-receiver functions are approximately 2 s and 5 s, respectively, representing typical dominant periods for observed data (normally 1–5 s for *P* and 4–10 s for *S*-receiver functions). For the synthetic *P* receiver functions, primary conversions appear together with multiple phases at positive times. The LAB converted phase, expected at a time of ~17 s, is effectively masked by the strong crustal multiples. For the synthetic SRFs, they occur on either side of 0 s and the LAB is clearly visible, although detailed crustal structures are not well resolved. As the velocity jump at the LAB becomes more gradational, its expression in the SRFs becomes weaker and broader. For a dominant period of approximately 5 s, SRFs appear to be able to resolve the LAB as a 50-km thick gradient zone (dashed lines). The *S*–*P* converted phase is dramatically weaker for a 100 km thick gradient zone (dotted line). Thus, in contrast to surface waves, *S*-receiver functions have the capability to distinguish between sharp and gradational LAB.

Below, we show an example which illustrates the complementary nature of SRFs and surface-wave data for mapping the LAB. Surface waves provide well-constrained estimates of absolute velocity in the lithosphere, but are insensitive to whether the LAB is gradational or abrupt. SRFs, on the other hand, can in principle be used to infer abruptness of the LAB relative to the seismic wavelength of 20–50 km, but lack good depth constraints. More work is required to test the SRF method in different cratonic settings, and to develop joint inversion methodologies that could exploit the complementary imaging characteristics of SRFs and surface waves.

5.1.6. Regional seismic studies of the LAB

5.1.6.1. Southern Africa. The cratons of southern Africa have been studied extensively in recent years, though the variation in data sets, methodology and methods of interpretation make a consistent review of the results difficult. The scope of surface-wave based models ranges from relatively low-resolution 3-D images derived from continental-scale studies (e.g., Priestley et al., 2006; Sebai et al., 2006) through craton-scale 1-D and 3-D models (e.g., Freybourger et al., 2001; Saltzer, 2002; Larson et al., 2006; Li and Burke, 2006) to detailed models of the internal structure of the Kaapvaal craton (Chevrot and Zhao, 2007). While the high-velocity lid beneath the Kaapvaal craton is a persistent feature of all surface-wave models, its depth extent and the nature of the mantle beneath the lid varies somewhat between the studies. The 1-D models of the Kaapvaal calculated from averaged dispersion data from the Southern African Seismic Experiment (Freybourger et al., 2001; Saltzer, 2002; Larson et al., 2006) are generally characterised by persistently high velocities, with no sublithospheric low-velocity zone required by the data.

Priestley et al. (2006) modelled shear-wave velocity structure and azimuthal anisotropy for the entire region of southern Africa. A widespread fast anomaly appears throughout southern Africa at 150 km depth, extending to ~200 km depth beneath the cratons. At

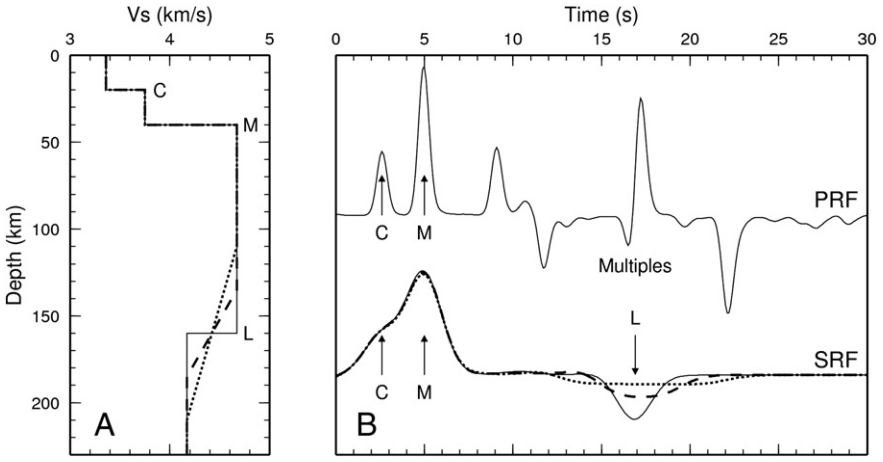

Fig. 12. Synthetic *P* and *S*-receiver functions for models with different LAB sharpness. (A) Three shear-wave velocity models, in which the LAB is a first-order discontinuity (solid line), a gradient zone of 50 km thick (dashed line), or a gradient zone of 100 km thick (dotted line). The Vp/Vs ratio is fixed to 1.73 in the crust and 1.80 in the mantle. C — Conrad interface, M — Moho, L — LAB. (B) Corresponding synthetic *P* and *S*-receiver functions. *S*-receiver functions are generated for models in (A) with identical line styles. *P* receiver function is only calculated for the model with an abrupt LAB. Timing is referred to a slowness of 6.4 s/deg. The frequency content of the synthetic receiver functions is approximately identical with that of observed data. For the *S*-receiver function we have reversed the amplitudes as well as the time axis to enable a direct comparison with *P* receiver function. Arrows (labeled C, M and L) indicate primary *P*-to-*S* conversions in the *P* receiver function and *S*-to-*P* conversions in the *S*-receiver functions. Unmarked phases with significant amplitudes in the *P* receiver function are crustal multiples. The multiple phases in the *S*-receiver function appear at the negative time, which are not shown.

250 km depth, velocities are slightly lower than the global reference model used in the study. Calculation of an average geotherm for the region from analysis of xenoliths gave a mechanical boundary layer thickness of 186 km and a depth of 204 km for the base of the thermal lithosphere, showing broad agreement with the depth range of high seismic velocities. The study of Sebai et al. (2006) covered a larger area – the entire African continent – and used a more comprehensive data set, including analysis of both Rayleigh and Love waves to characterise both velocity anomalies and radial and azimuthal anisotropy. Beneath the southern African cratons, the models showed velocities above those of global reference models, with the percentage anomaly highest in the uppermost mantle and decreasing gradually to 1% positive anomaly at 280 km depth. Radial anisotropy has a similar gradual decrease with depth over the range in which the data have sensitivity. The authors note a change in the nature of azimuthal anisotropy at ~180 km depth for all the African cratons, and attribute this feature to the signature of the cratonic root. The authors also attribute their anisotropy pattern at a depth of 280 km to the southern African superswell. Identification of the LAB on the basis of seismic velocity is not made.

In contrast, the 1-D and 3-D models of Li and Burke (2006), which model velocity variations across the SASE (Southern African Seismic Experiment) array, require the presence of a pervasive but weak low-velocity zone in the depth range ~160–260 km (Fig. 13). Using absolute velocity contours of 4.55–4.6 km/s as a proxy for the base of the lithosphere, Li and Burke (2006) estimated an ~180 km depth for the LAB, broadly consistent with estimates derived from analysis of xenoliths across the region. They also note that the nature of the velocity model does not allow a meaningful estimate of lithospheric thickness based on negative velocity gradients. The weak LVZ is interpreted as a thermal transition layer in which mantle convection is able to occur.

Data from the SASE array were used in a finite-frequency tomographic study by Chevrot and Zhao (2007), in which the tomographic method allowed the finer-scale internal structure of the Kaapvaal craton to be investigated. The Kaapvaal craton was shown to be heterogeneous in nature, with a distinct division into western and eastern blocks and variations in the thickness and nature of the high-velocity cratonic root. The models show a positive velocity anomaly extending to at least 250 km depth beneath parts of the Kaapvaal craton, though the nature of the reference model is not stated clearly. The authors note that the limited depth resolution of the study precludes definite conclusions regarding the thickness of the cratonic lithosphere.

Kumar et al. (2007) calculated *S*-receiver functions for a number of permanent stations in the Indian Ocean and adjacent continental regions. They showed a profile constructed using SRFs, for a set of stations extending from south to north in Africa (Fig. 14). Both the Moho and LAB are evident as discrete events that can be correlated across the profile. The polarity of the LAB is opposite to that of the Moho, since the LAB represents an upward increase in velocity whereas the Moho represents an upward velocity decrease. The LAB is clearly deeper (up to ~300 km) and weaker beneath cratonic regions of southern Africa than in other parts of the profile. This reduction in amplitude of the *P*–*S* mode conversion may reflect either a reduction in the parameter contrast at the LAB, or a less abrupt (more gradational) LAB beneath cratonic regions.

5.1.6.2. The Slave craton. Recent studies of shear shear-wave velocity and anisotropy using Rayleigh waves and *SKS* splitting measurements have provided new models of the lithospheric structure of the Slave craton. The studies of Snyder and Bruneton (2007) and Chen et al. (2007) use teleseismic data from the POLARIS broadband array deployed around the diamond-producing region in the centre of the Slave craton. Chen et al. (2007) used an array analysis technique to derive an average dispersion curve and average depth-dependent azimuthal anisotropy for the entire array, and inverted the dispersion data for shear-wave velocity structure. The resulting velocity–depth profile shows a high-velocity lid extending from the uppermost mantle to depths of 150–200 km, underlain by a negative velocity gradient with a minimum at ~275 km depth. The authors interpret the negative velocity gradient as the transition from lithosphere to asthenosphere. The centre of the gradient lies at ~220 km but the gradational nature of the transition and the sensitivity range of the surface-wave data set are such that the lithosphere–asthenosphere boundary cannot be identified with certainty; the authors note that it must lie at more than 150 km depth, and that a thick lithosphere (~250 km) cannot be ruled out by the data. The surface-wave analysis suggests north–south trending azimuthal anisotropy in the uppermost lithosphere and NE–SW to E–W trending azimuthal anisotropy in the lower lithosphere and sublithosphere.

Snyder and Bruneton (2007) used joint interpretation of SKS and surface-wave data for the southeastern section of the POLARIS Slave array to infer a two-layered system of anisotropy, with a north–south

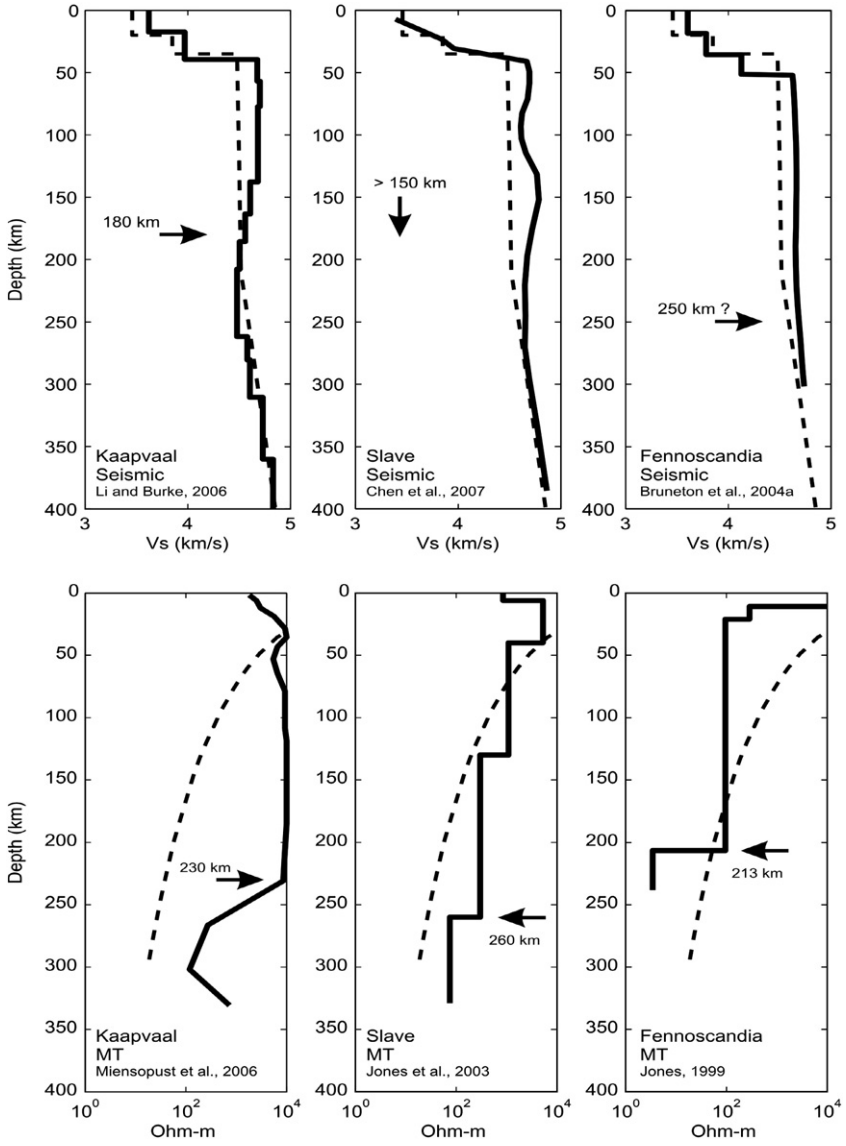

Fig. 13. Representative 1-D velocity and resistivity models for the three study regions. Arrows mark interpreted lithospheric thickness. Top panels show recent surface-wave results; dashed curve is model AK135. Lower panels show resistivity profiles for various MT studies; dashed curve is model REF from Jones, 1999. MT profile for Kaapvaal is extracted from the region of maximum lithospheric thickness from a preliminary 2-D inversion along a north–south MT transect through the central Kaapvaal craton (Miensopust et al., 2006). Slave MT profile represents an average for the Slave craton and may be biased toward slightly thicker lithosphere due to the station distribution in the Slave craton. Fennoscandia MT profile is for station NAT.

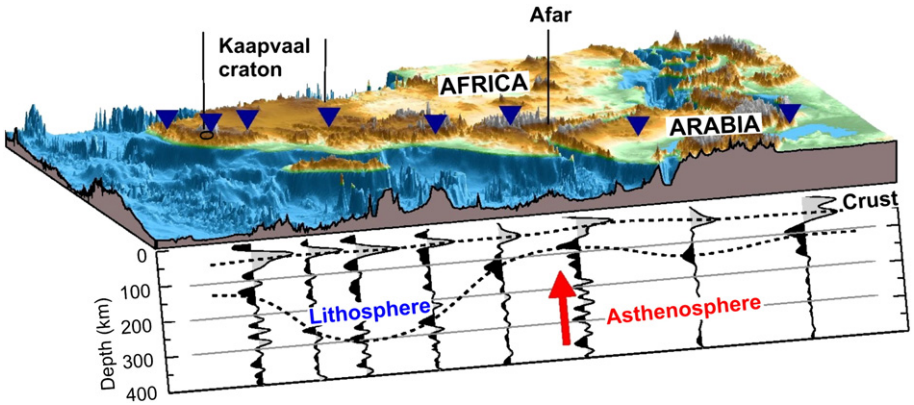

Fig. 14. *S*-receiver function cross section beneath Africa, showing the variation of lithospheric thickness between Precambrian shields and the tectonically active Afar region. The deepest lithospheric keel is observed beneath the Archean Kaapvaal craton. Positive amplitudes are shaded in gray and negative amplitudes are shaded in black, indicating a velocity increase or decrease, respectively. Triangles on the top denote seismic stations. (For interpretation of the references to colour in this figure legend, the reader is referred to the web version of this article.)

trend in the upper layer and a northeast trend in the lower layer. Forward modelling was used to test a number of hypotheses for the depth range and cause of the anisotropic signature. The upper layer is geologically consistent with a major phase of Archean deformation, but the deeper layer is more complex and controversial in origin. The fast direction of the lower layer is aligned with present-day plate motion and may result from anisotropy in both the lower lithosphere and sublithospheric mantle. Within the lower lithosphere, tests showed that the anisotropy could be explained either in terms of sheeted dykes that feed the Slave kimberlite eruptions, or in terms of a layer of underthrust Archean lithosphere. The authors do not explicitly consider the lithosphere–asthenosphere boundary, but the velocity model derived from the surface-wave dispersion data shows a high-velocity lid with a negative gradient beneath it and a velocity minimum at ~200 km depth. The models of layered anisotropy placed the base of the lithosphere at ~190–200 km depth.

5.1.6.3. The Fennoscandian Shield. The SVEKALAPKO seismic project sampled a 500×800 km^2 region of the Fennoscandian Shield in southern Finland, and included a large number of broadband seismographs recording data during 1998–1999. The results of array-based surface-wave studies of the region were presented by Bruneton et al. (2004a,b) and Pedersen et al. (2006). Bruneton et al. (2004a) derived an average 1-D dispersion curve for Rayleigh-wave phase velocities, inverted the dispersion data for isotropic shear-wave velocity structure and compared the results to shear-wave velocity profiles derived from xenolith compositional data for the region. The authors noted that the surface-wave model shows near-constant shear-wave velocity to depths of ~200 km, below which a positive velocity gradient was modelled. There was no clear low-velocity zone that could be attributed to the lithosphere–asthenosphere boundary anywhere within the 300 km depth range resolved by the surface-wave study. This is consistent with the work of Sandoval et al. (2004), who used body-wave tomography to document a high-velocity anomaly extending to at least 250 km depth beneath the central part of the Fennoscandian Shield, as well as results obtained by Hjelt et al. (2006) using various seismic techniques.

Three-dimensional shear shear-velocity modelling carried out by Bruneton et al. (2004b) showed significant lateral heterogeneity across the region, interpreted to arise from compositional variations within the lithospheric mantle. The authors noted that it may be possible to identify the LAB by a pronounced reduction of the lateral heterogeneity across a study region; however, the lateral resolution of the SVEKALAPKO study was insufficient below 150 km to test this hypothesis. Radial anisotropy was resolved to ~200 km depth by analysis of the Love–Rayleigh discrepancy. The observed anisotropy fabric requires a lithospheric structure in which olivine *a*-axes are oriented approximately horizontally and the composition is required to include at least 50% olivine. Average azimuthal anisotropy is weak above ~200 km but significant below ~200–250 km with an average alignment of 0–40°. Using information from surface and body body-wave studies, the authors suggested that the apparently weak lithospheric anisotropy may arise from complex lateral and vertical variation that averages to a low value over the resolution length of the surface waves. The deeper anisotropy was interpreted as arising from sublithospheric flow, but the discrepancy between the fast direction and the direction of absolute plate motion suggests that the pattern of sublithospheric flow beneath the Fennoscandian Shield may be complex.

6. The electrical lithosphere

6.1. ELAS layer

Electrical conductivity (or its inverse, resistivity) provides an important constraint on mantle structure that is independent of those obtained using seismological, or other geophysical, techniques. The bulk conductivity of the mantle is primarily controlled by temperature and composition (e.g., Xu et al., 2000; Ledo and Jones, 2005), but can be dramatically enhanced by the presence of an interconnected conducting phase such as melt or graphite, which is typically a minor constituent of the rock matrix. For these reasons, conductivity in the mantle lends itself to the identification of key upper upper-mantle boundaries, both vertically and laterally.

The magnetotelluric (MT) method is well suited to the problem of inferring Earth structure at mantle depths (e.g., Jones, 1999). The lithospheric mantle represents a relatively resistive layer (1000 s to 10,000 s Ω m) beneath a (typically) conductive lower crust. From the earliest MT studies on continents, it has been recognized that an increase in upper-mantle conductivity in the 50–250 km depth range (the electrical asthenosphere) is required to explain the observed frequency dependence of apparent resistivity at long periods. This layer was studied globally by many groups in the late-1970s and 1980s as part of the IUGG's (International Union of Geodesy and Geophysics) Inter-Association Working Group on Electromagnetic Lithosphere–Asthenosphere Soundings (ELAS) formed in 1983. Gough (1987) gave an interim report of the activities of the ELAS group.

Determination of mantle resistivity directly below the Moho to depths of about 100 km is hampered by pervasive highly-conductive lower crust that acts as a screen (Jones, 1999). Although the absolute conductivity of the lithospheric mantle is poorly constrained, the thickness of the resistive layer is well resolved, since the MT response is highly sensitive to the separation between the two conductive layers (Jones, 1999). In some places, however, there are resistive crustal "windows" through which the lithospheric mantle resistivity–depth profile can be reasonably well resolved although, once again, determining the actual resistivity of the most resistive part of the profile is virtually impossible — only a lower bound can be put on it. The most resistive upper mantle reported in the literature is that beneath the Rae Province of the Canadian Shield, adjacent to the Slave craton, where resistivities in excess of 65,000 Ω m have been reported by Jones et al. (2002) in a region of little crustal conductance.

Globally, comparisons with seismic data have shown, as early as 1963 (Ádám, 1963; Fournier et al., 1963), that the electrical asthenosphere accords well spatially and in depth with the seismically-defined asthenosphere (e.g., Calcagnile and Panza, 1987; Praus et al., 1990; Jones, 1999). Typical values quoted for the resistivity of the electrical asthenosphere are in the range of 5–25 Ω m, whereas at depths of 200–250 km a dry mantle mineralogy on an adiabat will yield a resistivity of hundreds of Ω m (Xu et al., 2000).

6.2. Regional MT studies

6.2.1. Kaapvaal craton

The Southern African Magnetotelluric Experiment (SAMTEX) is an ongoing large-scale MT investigation of electrical structure of the crust and upper mantle beneath the Archean cratons of southern Africa and their surrounding terranes (Jones et al., 2004; Hamilton et al., 2006). SAMTEX deployments traverse the Kaapvaal craton in several directions (Fig. 2A). Using data from the main SW–NE profile, Hamilton et al. (2006) showed that the direction of maximum conductivity in the upper mantle (geoelectric strike) is incompatible with seismic anisotropy inferred from SKS splitting studies (Silver et al., 2004). This scenario, like the contrast between isotropic electrical structure and seismic anisotropy in the Superior craton noted by Hirth et al. (2000), suggests that the mantle fabric responsible for seismic anisotropy in southern Africa has either a weak electrical anisotropic signature, or is located at a depth greater than the maximum depth (150+ km) of investigation of Hamilton et al. (2006).

Jones et al. (2004) presented a preliminary 2-D long-period MT model for the same SW–NE transect across the Kaapvaal craton. A prominent keel-shaped lithospheric root beneath the Kaapvaal is imaged by their model, similar in shape to the LAB structure inferred

from *S*-receiver functions in the same region (Fig. 14). As a general indication of regional resistivity structure, a 1-D resistivity–depth profile extracted near the thickest part of the root from their preliminary model shows a sharp reduction in electrical resistivity at a depth of ~230 km (Fig. 13). This – and other resistivity profiles in Fig. 13 – are compared with a reference model for the mantle obtained by Jones (1999).

6.2.2. Slave craton

The electric structure of the lithosphere beneath the Slave craton has been extensively studied using data from LITHOPROBE and related experiments (e.g., Jones et al., 2001; 2003). These MT surveys used ocean-bottom instruments deployed by float planes into lakes (circles in Fig. 2B), as well as conventional land-based MT units (squares), deployed both in the summertime and also on lakes in wintertime. Although the MT experiments were initially designed to image the LAB, they led to the discovery of an unusual conductive region at depths of 80–120+ km (the Central Slave Mantle Conductor; CSMC) that is spatially coincident with a geochemically defined ultra-depleted harzburgitic layer (Jones et al., 2001; 2003). The inferred base of the CSMC possibly coincides with the graphite–diamond boundary, suggesting that carbon interconnected along grain boundaries may represent the conductive mantle phase (Jones et al., 2003).

Using the average MT response for stations distributed throughout the Slave craton, Jones et al. (2003) showed that a minimum of five homogeneous layers are required to fit the data. Based on their average model (see Fig. 13), the electrical LAB beneath the Slave craton is located on average at 260 (225–310) km and represents a decrease from 300 (150–600) Ωm to 75 (55–95) Ωm. Noting that the majority of the MT stations are located in the southern Slave region, Jones et al. (2003) suggested that the lithospheric thickness at Lac de Gras in the centre of the craton, is less than this value based on the data from the ocean-bottom instrument located in the lake. A LAB at around 200 km is suggested by Jones et al. (2003), consistent with petrological observations (Pearson et al., 1999).

6.2.3. Fennoscandia

A number of studies have demonstrated that seismic and electrical LAB approximately coincide beneath the Fennoscandian Shield (see Jones et al., 1983; Jones, 1999), although recent array data show that the shield has complex electrical structure (Hjelt et al., 2006), possibly including anisotropy. Fig. 13 shows a resistivity profile obtained by Monte-Carlo search approach (Jones and Hutton, 1979) of summertime MT recordings at station NAT (Jones et al., 1983). The estimated thickness of the lithosphere at this western site is 213 + 26/− 23 km (Jones et al., 1999). Although early studies suggested that no well developed electrical asthenosphere exists in the Karelian craton in central Finland (Korja, 1993), more recent work within the framework of the Baltic Electromagnetic Array Research (BEAR) project (Engels et al., 2002; Lahti et al., 2005; Hjelt et al., 2006) has provided new insights. Multi-sheet modelling of MT response (Engels et al., 2002) shows that inclusion of an electrical asthenosphere with resistivity of 20 20 Ωm at a minimum depth between 200–300 km significantly improves the fit to the data. Lahti et al. (2005) noted that although numerous highly conductive crustal bodies and conductivity contrasts produce strong distortions, a decrease in resistivity is required at depths greater than 170 km, providing a minimum depth estimate for the electrical LAB. Korja (2007) recently presented an updated map of lithospheric thickness for Scandinavia, based on a compilation of older and newer sources. His map shows significant variation within Fennoscandia from ca. 170 to >300 km, with the greatest thickness in the region of the Karelian craton where the kimberlites are located. Within the area covered by the SVELALAPKO seismic array, the MT data appear to require an increase in mantle conductivity at some depth beneath 200 km, although the data do not constrain the depth and geometry of this conducting layer (Hjelt et al., 2006).

7. Discussion

Material from the cratonic upper mantle entrained by kimberlites shows that depleted cratonic peridotite samples typically occur on steady-state conductive geotherms to pressures of 46 to 50 kbar. Although commonly exposed to thermal disturbance and textural modification, suggesting they may represent a dynamically evolving transition layer in the lower lithosphere, xenoliths from greater depths retain relict depleted compositions and Archean isotopic characteristics even to the most extreme pressures represented in the available data set (~65 kbar). Thus, although modern single-grain thermobarometry techniques have increased the observational data base by orders of magnitude, there are still no reported major-element mineral compositions that can be taken to represent unambiguously the "asthenosphere" that must underlie Archean cratonic roots. In order to map the LAB, a geophysical approach is thus required.

For the three cratons considered in this study, the depth of the LAB is found to vary broadly between 150 and 300 km (Table 2). We remark that such comparisons are fraught with uncertainty, arising (among other things) from large spatial variations in lithospheric thickness beneath cratons (e.g., Artemieva and Mooney, 2002). Nevertheless, our comparisons of LAB depth provide some support for previously inferred consistency of seismic and MT methods (e.g., Calcagnile and Panza, 1987; Praus et al., 1990; Jones, 1999), and demonstrate the compatibility of these results with inferences of lithospheric thickness from creep modelling. Seismic inferences exhibit a greater scatter than those from MT studies, no doubt reflecting the subtle expression of the LAB beneath cratons in surface-wave velocity models as well as the paucity of *S*-receiver-function analyses in these regions. Although not explicitly considered in Table 2, global and regional studies (e.g., Gaherty and Jordan, 1995; Gung et al., 2003; Debayle et al., 2005) suggest that depth variations in seismic anisotropy may also be used as a marker of the LAB. In terms of our creep results, such changes in anisotropy may represent a transition from "frozen" anisotropy in the lithosphere to recently developed fabrics within a dislocation-dominated creep regime at the base of the plate.

The causes of reduction in electrical resistivity and seismic shear velocity (if any) beneath the lithosphere have long been debated in the literature. For cratons with thick mantle roots, graphite along grain boundaries can be ruled out as an explanation for the electrical asthenosphere, since the graphite–diamond stability boundary occurs at lower pressure than the LAB (Kennedy and Kennedy, 1976). On the other hand, partial melt may provide a viable mechanism, since it increases electrical conductivity due to the high mobility of charge carriers within a melt fraction (Waff, 1974). Furthermore, it has long

Table 2
Summary of representative lithospheric thickness estimates for the three cratons

	Kaapvaal	Slave	Fennoscandia[a]
Xenolith (thickness of TBL)	>195–215 km	>170–215 km	>245 km
Strain rate $>10^{-15}$ s^{-1} under dry conditions[b]	245 km	235 km	220 km
Seismic	180 km (Li and Burke, 2006)	>150 km (Chen et al., 2007)	Consistent with 250 km (Bruneton et al., 2004a)
S-Receiver function	~250–300 km (Kumar et al., 2007)		
Magnetotelluric (MT)	230 km (Miensopust et al., 2006)	210 km at LdG 260 km average (Jones et al., 2003)	205 km at NAT (Jones, 1999) >300 km (Korja, 2007)

Uncertainties vary between methods and are generally >10 km.

[a] For Fennoscandia the xenolith–xenocrysts data are from the Archean–Proterozoic border, seismic data are from both domains (although mainly in the central part of the shield), and MT data are from Proterozoic regions.

[b] Estimates for wet conditions are not given, as they depend critically on the assumed depth distribution of water.

been suggested (e.g., Anderson and Sammis, 1970) that a reduction in seismic velocity at asthenospheric depths may be caused by small amounts of partial melt. Karato and Jung (1998), however, argue that melt in the asthenosphere is unlikely to impact seismic velocity, since there is a trade-off between an increase in velocity of the depleted matrix and a reduction in velocity caused by the melt itself. Melting will cause similar trade-offs for electrical conductivity, with the degree of interconnectivity of the melt critical for determining its impact on bulk conductivity. Competing observations have been reported about the degree of partial melt required for efficient interconnectivity (and thus a detectable reduction in electrical resistivity), from values as low as 0.02% (Drury and FitzGerald, 1996) to values of 2–3% (Faul, 1997; ten Grotenhuis et al., 2005). Drury and FitzGerald (1996) observed that very thin (1.0–1.5 nm) films can be found on grain boundaries that can only be observed using high-resolution electron microscopy and are not observable by light or SEM observations. These films form 0.02% of the fraction of the rock and are highly interconnected. In addition, small melt fractions along grain boundaries may be particularly important for carbonatitic melts; these may be interconnected at the 0.03–0.30% level (Dasgupta and Hirschmann, 2006).

Any degree of partial melt in the asthenosphere must be reconciled with models showing that the transition from a conductive geotherm onto a mantle adiabat generally occurs well below the dry solidus (e.g., Katz et al., 2003). The presence of volatiles in the mantle provide a possible mechanism for reducing the solidus temperature. For example, using a geotherm for the Kaapvaal craton that is based on heat flow data (Jones, 1988), and using theoretical melting relationships for the mantle as a function of temperature, pressure and water content (Katz et al., 2003), it is possible to estimate the minimum water contents needed for melting to be induced. Above ~150 km, the geotherm lies below the saturated solidus, and so melting here cannot occur without a thermal perturbation. At ~150 km a water content of ~0.3 wt% is needed for melting, and this amount decreases steadily with depth to around 0.2 wt% at 250 km. The laboratory data required to confirm these quantities do not exist, however, and so there is considerable variance in estimates of unsaturated wet solidii (G. Gaetani — pers. comm. with RLE). The possibility that the presence of CO_2 might further depress the solidus has also been raised (Dasgupta et al., 2007). Recent analysis of water solubility in aluminous pyroxenes suggests a correlation between a minimum in water solubility and the top of the global seismic low-velocity zone (Mierdel et al., 2007), both for oceanic and continental geotherms, providing a possible link between water content and low velocities. In this model, the release of even quite small amounts of water from aluminous OPX is deemed sufficient to induce melting.

Alternatively, water, in the form of dissolved hydrogen, has been invoked to explain elevated conductivities in the oceanic mantle (Lizarralde et al., 1995; Evans et al., 2005) and in the asthenosphere beneath continents (Hirth et al., 2000). Although there is still some disagreement between different laboratory measurements, the balance of evidence suggests that hydrogen enhances conductivity (Yoshino et al., 2006; Wang et al., 2006). Calculations suggest that the transition from dry lithospheric mantle to a "damp" asthenosphere (Hirth et al., 2000) would result in about an order-of-magnitude increase in conductivity (Karato 1990; Hirth and Kohlstedt 2003). In the presence of modest water content, the transition from a dry lithosphere to a wet asthenosphere could be quite broad (Lee et al., 2005).

The amount of water present in the mantle (both lithospheric and asthenospheric) remains controversial and is a question that is being debated fiercely within various communities. For example, Berry et al. (2005) question the applicability of experimental studies that constrain mantle water contents (e.g., Karato and Jung, 1998; Hirth and Kohlstedt, 2003), arguing that to be applicable such experiments must be undertaken on olivine that contains the hydrated defects appropriate for the part of the mantle being investigated. Walker et al. (2007) discuss the intricacies of the four different mechanisms by which hydrogen can be incorporated into the crystal structure of olivine. Although this topic extends beyond the scope of this paper, establishing the abundance, distribution and role of water in the asthenosphere is clearly of fundamental significance to understanding the nature of the LAB beneath cratons.

8. Conclusions

Thermobarometry of mantle xenoliths and xenocrysts entrained in kimberlite provide a stratigraphic framework for studies of the mantle lithosphere beneath three Archean regions (the Kaapvaal craton, the Slave craton and the Fennoscandian Shield) and provide minimum thickness estimates for the thermal boundary layer (170–245 km), but only indirect constraints for interpretation of the nature of the lithosphere–asthenosphere boundary. In northern Lesotho, a lithospheric 'type' section is defined by coarse-textured xenoliths with strongly depleted composition that cluster along a 40 mW/m^2 conductive geotherm. A subset of northern Lesotho xenoliths record unique supra-adiabatic temperatures at 53–61 kbar (200–230 km depth), interpreted to result from advection of asthenosphere-derived melts and heat into the TBL. Near Kimberley, the Frank Smith kimberlite hosts deformed, high-temperature peridotites with depleted composition. These samples record transient thermal disturbances, but also lack asthenospheric composition and isotopic characteristics. The cratonic mantle underlying the Lac de Gras kimberlites in the central Slave craton, Canada is compositionally layered. Here, depleted peridotite exists throughout the section to the deepest levels represented, with no trace of FO89 asthenospheric olivine compositions even at temperatures close to the adiabat. In Finland, xenoliths from close to the margin between the Archean Karelian craton and Proterozoic Svecofennian belt are dominated by lherzolitic olivine with depleted FO91 to FO93 composition. No asthenophere is apparent in a mantle section that extends to near-adiabatic temperatures at pressures up to ~65 kbar (~245 km). Taken together, xenolith and xenocryst suites from these three cratons suggest that xenolith thermobarometry techniques tend to underestimate the depth extent of time-averaged petrologic lithosphere, due in part to the prevalence of deep-seated thermal and compositional disturbances attending kimberlite magmatism.

Present-day differential motion between the lithosphere and asthenosphere is accommodated by mantle creep. Based on recently revised olivine creep parameters (Korenaga and Karato, 2008) and assuming an average grain size of 1 cm, consistent with coarse textures observed in cratonic xenoliths, the dominant deformation mode near (and beneath) the LAB is expected to be dislocation creep. In contrast to diffusion creep, this mechanism leads to a lattice-preferred orientation that may be observed as seismic or electrical anisotropy that will overprint any older fabrics. Under dry conditions in the lithosphere and asthenosphere, the LAB is thermally controlled and diffuse in character. A uniform shear stress of more than 2 MPa (20 bars) is required, and most of the differential motion between the lithosphere and asthenosphere is accommodated within a ~50 km thick region of high strain rate in the asthenosphere. Under "damp" conditions (C_{OH}>100 ppm) the LAB is mainly regulated by water content and appears to be more abrupt in character. The required stress level falls to <0.5 Mpa (5 bars), and differential motion is accommodated within a broad asthenospheric zone that extends from the LAB to the top of the mantle transition zone.

Velocity models derived from surface-wave studies give some indication of the transition from lithosphere (characterised as a lid of anomalously high shear-wave velocity) to asthenosphere, but are unable to resolve sharp discontinuities directly. In the absence of a clear LAB signal, a variety of proxy estimates for lithospheric thickness is used, most commonly based either on negative velocity gradients at the base of the lithospheric lid or the convergence of the seismic-velocity profile with that of global reference models. Where depth-dependent seismic anisotropy has been studied using surface-wave

data, it has been possible to interpret the presence of a "mechanical" LAB, based on craton/continent-wide organization of azimuthal anisotropy. *S*-receiver functions have the potential to resolve the seismic LAB with higher resolution than surface waves, but have yet to be applied in many cratonic settings. Available data from southern Africa suggest that the seismic LAB beneath cratons is more diffuse than in other tectonic settings.

The electrical LAB is manifested as a significant reduction in electrical resistivity, from the lithosphere into the asthenosphere. The thickness of the resistive lithosphere is relatively well determined by magnetotelluric (MT) observations. Previous compilations have demonstrated that the electrical asthenosphere is in good agreement with seismically-defined low-velocity zones (e.g., Calcagnile and Panza, 1987; Praus et al., 1990; Jones, 1999). Based on laboratory studies of electrical conductivity in mantle rocks, this change in conductivity at the LAB may be explained by either partial melt or the presence of small amount of water in the mantle. The amount of water in the mantle remains a hotly debated topic.

For the three studied cratons, the depth of the electrical LAB is found to vary from ~205 km (minimum for Fennoscandia) to as much as 230 km (Kaapvaal). These depth estimates are generally consistent with lithospheric thickness derived from mantle creep modelling and available constrains on thickness of the TBL based on xenolith thermobarometry (Table 2). Current seismic depth estimates exhibit a greater degree of scatter, probably reflecting the subtle character of the seismic LAB beneath cratons. Nevertheless, the overall agreement obtained using different proxies provides encouragement that effective geophysical tools exist to map the elusive LAB beneath cratons.

Acknowledgements

The organizers (Helle Pedersen, Nicholas Arndt, David Snyder, Don Francis and Tom Jordan) of a workshop on 8–11 March, 2007 entitled "The Structure of the Lithosphere: the Petro-Geophysical Approach" are sincerely thanked for creating a venue for highly stimulating discussion, which provided the motivation for this work. Jun Korenaga is thanked for providing a preprint of a paper containing new analyses of olivine creep parameters.

References

Ádám, A., 1963. Study of the electrical conductivity of the Earth's crust and upper mantle. Methodology and results. Dissertation. Sopron, Hungary.
Anderson, D.L., Sammis, C., 1970. Partial melting in the upper mantle. Physics of the Earth and Planetary Interiors 3, 41–50.
Armstrong, J.P., 2001. Kimberlite Indicator Mineral Chemistry Database (KIMC): a preliminary digital compilation of Kimberlite Indicator Mineral Chemistry extracted from publically available assessment filings; Slave Craton and environs, Northwest Territories and Nunavut, Canada. DIAND NWT Geology Division, DIAND EGS Open Report 2001-02 (CD-ROM).
Artemieva, I.M., Mooney, W.D., 2002. On the relation between cratonic lithosphere thickness, plate motions, and basal drag. Tectonophysics 358, 211–231.
Babuška, V., Plomerová, J., 2006. European mantle lithosphere assembled from rigid microplates with inherited seismic anisotropy. Physics of the Earth and Planetary Interiors 158, 264–280.
Barrell, J., 1914. The strength of the Earth's crust. Journal of Geology 14, 28–48.
Behn, M.D., Conrad, C.P., Silver, P.G., 2004. Detection of upper mantle flow associated with the African Superplume. Earth and Planetary Science Letters 224, 259–274.
Bell, D.R., Rossman, G.R., 1992. Water in Earth's mantle: the role of nominally anhydrous minerals. Science 255, 1391–1397.
Berry, A.J., Hermann, J., O'Neill, H.S.C., Foran, G.J., 2005. Fingerprinting the water site in mantle olivine. Geology 33, 869–872. doi:10.1130/G21759.1.
Bock, G., Kind, R., 1991. A global study of S-to-P and P-to-S conversions from the upper mantle transition zone. Geophysical Journal International 107, 117–129.
Bokelmann, G., Silver, P., 2002. Shear stress at the base of shield lithosphere. Geophysical Research Letters 29. doi:10.1029/2002GL015925.
Boyd, F.R., Nixon, P.H., 1978. Ultramafic nodules from the Kimberley pipes, South Africa. Geochimica et Cosmochimica Acta 42, 1367–1382.
Boyd, F.R., Gurney, J.J., 1982. Low-calcium garnets: keys to craton structure and diamond crystallization. Carnegie Institution of Washington Yearbook 81, 261–267.
Brey, G.P., Kohler, T., 1990. Geothermobarometry in four-phase lherzolites II, new thermobarometers, and practical assessment of existing thermobarometers. Journal of Petrology 31, 1353–1378.
Brune, J., Dorman, J., 1963. Seismic waves and earth structure in the Canadian Shield. Bulletin of the Seismological Society of America 53, 167–210.
Bruneton, M., Pedersen, H.A., Vacher, P., Kukkonen, I.T., Arndt, N.T., Funke, S., Friederich, W., Farra, V., SVEKALAPKO Seismic Tomography Working Group, 2004a. Layered lithospheric mantle in the central Baltic Shield from surface waves and xenolith analysis. Earth and Planetary Science Letters 226, 41–52.
Bruneton, M., et al., 2004b. Complex lithospheric structure under the central Baltic Shield from surface wave tomography. Journal of Geophysical Research 109, B10303. doi:10.1029/2003JB002947.
Calcagnile, G., Panza, G.F., 1987. Properties of the lithosphere–asthenosphere system in Europe with a view towards Earth conductivity. Pure and Applied Geophysics 125, 241–254.
Ceuleneer, A., Nicolas, F., Boudier, F., 1988. Mantle flow patterns at an oceanic spreading centre: the Oman peridotites record. Tectonophysics 151, 1–26.
Chen, C.-W., Rondenay, S., Weertatatne, D.S., Snyder, D.B., 2007. New constraints on the upper mantle structure of the Slave craton from Rayleigh wave inversion. Geophysical Research Letters 34, L10301. doi:10.1029/2007GL029535.
Chen, L., Zheng, T., Xu, W., 2006. A thinned lithospheric image of the Tanlu Fault Zone, eastern China constructed from wave equation based receiver function migration. Journal of Geophysical Research 111, B09312. doi:10.1029/2005JB003974.
Chevrot, S., Zhao, L., 2007. Multiscale finite-frequency Rayleigh wave tomography of the Kaapvaal craton. Geophysical Journal International 169, 201–215.
Conrad, C.P., Lithgow-Bertelloni, C., 2006. Influence of continental roots and asthenosphere on plate–mantle coupling. Geophysical Research Letters 33. doi:10.1029/2005GL025621.
Cotte, N., Pedersen, H.A., TOR Working Group, 2002. Sharp contrast in lithospheric structure across the Sorgenfrei-Tornquist Zone as inferred by Rayleigh wave analysis of TOR1 project data. Tectonophysics 260, 75–88.
Creaser, R.A., Grütter, H., Carlson, J., Crawford, B., 2004. Macrocrystal phlogopite Rb–Sr dates for the Ekati property kimberlites, Slave province, Canada: evidence for multiple intrusive episodes in the Paleocene and Eocene. Lithos 76, 399–414.
Darbyshire, F.A., Eaton, D.W., Frederiksen, A.W., Ertolahti, L., 2007. New insights into the lithosphere beneath the Superior Province from Rayleigh wave dispersion and receiver function analysis. Geophysical Journal International 169, 173–1067.
Dasgupta, R., Hirschmann, M.M., 2006. Melting in the Earth's deep upper mantle caused by carbon dioxide. Nature 440, 659–662.
Dasgupta, R., Hirschmann, M.M., Smith, N.D., 2007. Water follows carbon: CO_2 incites deep silicate melting and dehydration beneath mid-ocean ridges. Geology 35, 135–138.
Debayle, E., Kennett, B.L.N., 2000a. The Australian continental upper mantle: structure and deformation inferred from surface waves. Journal of Geophysical Research 105, 25,423–25,450.
Debayle, E., Kennett, B.L.N., 2000b. Anisotropy in the Australasian upper mantle from Love and Rayleigh waveform inversion. Earth and Planetary Science Letters 184, 339–351.
Debayle, E., Kennett, B., Priestley, K., 2005. Global azimuthal seismic anisotropy and the unique plate-motion deformation of Australia. Nature 433, 509–512.
Dragoni, M., Pasquale, V., Verdoya, M., Chiozzi, P., 1993. Rheological consequences of the lithospheric thermal structure in the Fennoscandian Shield. Global and Planetary Change 8, 113–126.
Drury, M.R., FitzGerald, J.D., 1996. Grain boundary melt films in an experimentally deformed olivine–orthopyroxene rock; implications for melt distribution in upper mantle rocks. Geophysical Research Letters 23, 701–704.
Durham, W.B., Goetze, C., 1977. Plastic flow of oriented single crystals of olivine; 1, mechanical data. Journal of Geophysical Research 82, 5737–5753.
Eaton, D.W., Frederiksen, A., 2007. Seismic evidence for convection-driven motion of the North American plate. Nature 446, 428–431.
Engels, M., Korja, T., BEAR working group, 2002. Multisheet modelling of the electrical conductivity structure of the Fennoscandian Shield. Earth Planets & Space 54, 559–593.
Evans, R.L., Hirth, G., Baba, K., Forsyth, D., Chave, A., Mackie, R., 2005. Geophysical controls from the MELT area for compositional controls on oceanic plates. Nature 437, 249–252.
Farra, V., Vinnik, L., 2000. Upper mantle stratification by P and S receiver functions. Geophysical Journal International 141, 699–712.
Faul, U.H., 1997. Permeability of partially molten upper mantle rocks from experiments and percolation theory. Journal of Geophysical Research 102, 10299–10311.
Finnerty, A.A., 1989. Xenolith-derived geotherms: whither the inflection? Contributions to Mineralogy and Petrology 102, 367–375.
Finnerty, A.A., Boyd, F.R., 1987. Thermobarometry for garnet peridotites: basis for the determination of thermal and compositional structure of the upper mantle. In: Nixon, P.H. (Ed.), Mantle Xenoliths. Wiley & Sons, pp. 381–402.
Forte, A.M., Mitrovica, J.X., 1996. New inferences of mantle viscosity from joint inversion of long-wavelength mantle convection and post-glacial rebound data. Geophysical Research Letters 23, 1147–1150.
Forte, A.M., Perry, H.C.K., 2001. Geodynamic evidence for a chemically depleted continental tectosphere. Science 290, 1940–1944.
Fouch, M.J., Rondenay, S., 2006. Seismic anisotropy beneath stable continental interiors. Physics of the Earth and Planetary Interiors 158, 292–320.
Fournier, H.G., Ward, S.H., Morrison, H.F., 1963. Magnetotelluric evidence for the low velocity layer. Space Sciences Laboratory, University of California Series No. 4, Issue No. 76.
Frederiksen, A.W., Bostock, M.G., Cassidy, J.F., 2001. S-wave velocity structure of the Canadian upper mantle. Physics of the Earth and Planetary Interiors 124, 175–191.
Freybourger, M., Gaherty, J.B., Jordan, T.H., Kaapvaal Seismic Group, 2001. Structure of the Kaapvaal craton from surface waves. Geophysical Research Letters 28, 2489–2492.

Gaherty, J.B., 2004. A surface wave analysis of seismic anisotropy beneath eastern North America. Geophysical Journal International 158, 1053–1066.
Gaherty, J.B., Jordan, T.H., 1995. Lehmann Discontinuity as the base of an anisotropic layer beneath continents. Science 268, 1468–1471.
Gaherty, J.B., Kato, M., Jordan, T.H., 1999. Seismological structure of the upper mantle: a regional comparison of seismic layering. Physics of the Earth and Planetary Interiors 110, 21–41.
Gough, D.I. (editor), 1987. Interim report on Electromagnetic Lithosphere Asthenosphere Soundings (ELAS) to Co ordinating Committee No. 5 of the International Lithosphere Programme. In: Composition, Structure and Dynamics of the Lithosphere Asthenosphere System, eds., K. Fuchs and C. Froidevaux. AGU Mono., Geodynam. Ser. 16:. Publication 0135 of the International Lithosphere Program, 219 237.
Griffin, W.L., Smith, D., Ryan, C.G., O'Reilly, S.Y., Win, T.T., 1996. Trace element zoning in mantle minerals: metasomatism and thermal events in the upper mantle. Canadian Mineralogist 34, 1179–1193.
Griffin, W.L., Doyle, B.J., Ryan, C.G., Pearson, N.J., O'Reilly, S.Y., Davies, R., Kivi, K., van Achterbergh, E., Natapov, L.M., 1999. Layered mantle lithosphere in the Lac de Gras area, Slave craton: composition, structure and origin. Journal of Petrology 40, 705–727.
Griffin, W.L., O' Reilly, S.Y., Doyle, B.J., Pearson, N.J., Coopersmith, H., Kivi, K., Malkovets, V., Pokhilenko, N., 2004. Lithosphere mapping beneath the North American plate. Lithos 77, 873–922.
Gripp, A.E., Gordon, R.G., 2002. Young tracks of hotspots and current plate velocities. Geophysical Journal International 150, 321–361.
Grütter, H.S., Moore, R., 2003. Pyroxene Geotherms Revisited — an Empirical Approach Based on Canadian Xenoliths. Extended Abstract, Eighth International Kimberlite Conference, 272 (CD-ROM).
Grütter, H.S., Apter, D.B., Kong, J., 1999. Crust–mantle coupling: evidence from mantle-derived xenocrystic garnets. In: Gurney, J.J., Gurney, J.L., Pascoe, M.D., Richardson, S.H. (Eds.), J.B. Dawson Volume, Proc. 7th International Kimberlite Conference. Red Roof Design, Cape Town, pp. 307–313.
Grütter, H.S., Gurney, J.J., Menzies, A.H., Winter, F., 2004. An updated classification scheme for mantle-derived garnet, for use by diamond explorers. Lithos 77, 841–857.
Grütter, H., Latti, D., Menzies, A., 2006. Cr-saturation arrays in concentrate garnet compositions from kimberlite and their use in mantle barometry. Journal of Petrology 47, 801–820.
Gung, Y., Panning, M., Romanowicz, B., 2003. Global anisotropy and the thickness of continents. Nature 422, 707–711.
Gurney, J.J., 1984. A correlation between garnets and diamonds. In: Glover, J.E., Harris, P.G. (Eds.), Kimberlite Occurrence and Origin: a Basis for Conceptual Models in Exploration. Geology Department and University Extension. University of Western Australia, Publication 8, 143–166.
Hamilton, M., Jones, A.G., Evans, R.L., Evans, S., Fourie, S., Garcia, X., Mountford, A., Spratt, J.E., SAMTEX Team, 2006. Electrical anisotropy of South African lithosphere compared with seismic anisotropy from shear-wave splitting analyses. Physics of the Earth and Planetary Interiors 158, 226–239.
Hjelt, S.-E., Korja, T., Kozlovskaya, E., Lahti, I., Yliniemi, J., BEAR, SVEKALAPKO Seismic Tomography Working Groups, 2006. Electrical conductivity and seismic velocity structures of the lithosphere beneath the Fennoscandian Shield. In: Gee, D.G., Stephenson, R.A. (Eds.), European Lithosphere Dynamics, 32. Memoirs of the Geological Society of London, pp. 541–559.
Hirth, G., Kohlstedt, G.L., 2003. Rheology of the upper mantle and mantle wedge: a view from experimentalists. In: Eiler, J. (Ed.), Inside the Subduction Factor. American Geophysical Union, Washington, D.C, pp. 83–105.
Hirth, G., Evans, R.L., Chave, A.D., 2000. Comparison of continental and oceanic mantle electrical conductivity: is the archean lithosphere dry? Geochemestry, Geophysics, and Geosystems 1 paper no.2000GC000048.
Hoffman, P.F., 1988. United Plates of America, the birth of a craton: early Proterozoic assembly and growth of Laurentia. Annual Review of the Earth and Planetary Sciences 16, 543–603.
Hoffman, P.F., 1990. Geological constraints on the origin of the mantle root beneath the Canadian Shield. Philosophical Transactions of the Royal Society of London A 331, 523–532.
Jones, A.G., 1999. Imaging the continental upper mantle using electromagnetic methods. Lithos 48, 57–80.
Jones, A.G., Hutton, R., 1979. A multi-station magnetotelluric study in southern Scotland II. Monte-Carlo inversion of the data and its geophysical and tectonic implications. Geophysical Journal of the Royal Astronomy Society 56, 351–368.
Jones, A.G., Olafsdottir, B., Tiikkainen, J., 1983. Geomagnetic induction studies in Scandinavia — III. Magnetotelluric observations. Journal of Geophysics 54, 35–50.
Jones, A.G., Ferguson, I.A., Chave, A.D., Evans, R.L., McNeice, G.W., 2001. Electric lithosphere of the Slave craton. Geology 29, 423–426.
Jones, A.G., Snyder, D., Hanmer, S., Asudeh, I., White, D., Eaton, D., Clarke, G., 2002. Magnetotelluric and teleseismic study across the Snowbird Tectonic Zone, Canadian Shield: a Neoarchean mantle suture? Geophysical Research Letters 29 (17), 10–1 – 10-4. doi:10.1029/2002GL015359.
Jones, A.G., Lezeata, P., Ferguson, I.A., Chave, A.D., Evans, R.L., Garcia, X., Spratt, J., 2003. The electrical structure of the Slave craton. Lithos 71, 505–527.
Jones, A.G., Spratt, J., Horan, C., Wallace, G., Hamilton, M., Evans, R.L., Garcia, X., Chave, A.D., Stettler, E., Adlem, M., Stettler, R., Raath, K., Evans, S., SAMTEX MT Team, 2004. The electrical lithosphere of the Kaapvaal Craton: project SAMTEX overview and first results. Contributed Paper at: Geoscience Africa. Johannesburg, South Africa.
Jones, M.Q., 1988. Heat flow in the Witwatersrand Basin and environs and its significance for the South African Shield geotherm and lithosphere thickness. Journal of Geophysical Research 93, 3243–3260.
Jordan, T.H., 1975. The continental tectosphere. Reviews of Geophysics and Space Physics 13, 1–12.
Jordan, T.H., 1978. Composition and development of the continental tectosphere. Nature 274, 544–548.
Jordan, T.H., 1981. Continents as a chemical boundary layer. Philosophical Transactions of the Royal Society of London, Series A: Mathematical and Physical Sciences 301, 359–373.
Karato, S., 1990. The role of hydrogen in the electrical conductivity of the upper mantle. Nature 347, 272–273.
Karato, S., Wu, P., 1993. Rheology of the upper mantle: a synthesis. Science 260, 771–778.
Karato, S., Jung, H., 1998. Water, partial melting and the origin of the seismic low velocity and high attenuation zone in the upper mantle. Earth and Planetary Science Letters 157, 193–207.
Katz, R.F., Spiegelman, M., Langmuir, C.H., 2003. A new parameterization of hydrous mantle melting. Geochemistry, Geophysics, & Geosystems 4. doi:10.1029/2002GC000433.
Kennedy, C.S., Kennedy, G.C., 1976. The equilibrium boundary between graphite and diamond. Journal of Geophysical Research 81, 2467–2470.
Korenaga, J., Karato, S.-I., 2008. A new analysis of experimental data on olivine rheology. Journal of Geophysical Research 113, B02403. doi:10.1029/2007JB005100.
Korja, T., 1993. Electrical conductivity distribution of the lithosphere in the central Fennoscandian. Shield and Precambrian Research 64, 85–108.
Korja, T., 2007. How is the European lithosphere imaged by magnetotellurics? Surveys in Geophysics 28, 239–272.
Kukkonen, I.T., Peltonen, P., 1999. Xenolith-controlled geotherm for the central Fennoscandian Shield: implications for lithosphere–asthenosphere relations. Tectonophysics 304, 301–315.
Kumar, P., Yuan, X., Kind, R., Kosarev, G., 2005. Lithosphere–asthenosphere boundary in the Tien Shan-Karakoram region from S receiver functions: evidence for continental subduction. Geophysical Research Letters 32. doi:10.1029/2004GL022291.
Kumar, P., Yuan, X., Kind, R., Ni, J., 2006. Imaging the colliding Indian and Asian continental lithospheric plates beneath Tibet. Journal of Geophysical Research 111, B06308. doi:10.1029/2005JB003930.
Kumar, P., Yuan, X., Kumar, M.R., Kind, R., Li, X., Chadha, R.K., 2007. The rapid drift of the Indian Plate. Nature 449, 894–897.
Lahti, I., Korja, P., Kaikkonen, K., Vaittinen, K., BEAR working group, 2005. Decomposition analysis of the BEAR magnetotelluric data: implications for the upper mantle conductivity in the Fennoscandian Shield. Geophysical Journal International 163, 900–914.
Langston, C.A., 1977. Corvallis, Oregon, crustal and upper mantle structure from teleseismic P and S waves. Bulletin of the Seismological Society of America 67, 713–724.
Larson, A.M., Snoke, J.A., James, D.E., 2006. S-wave velocity structure, mantle xenoliths and the upper mantle beneath the Kaapvaal Craton. Geophysical Journal International 167, 171–186.
Ledo, J., Jones, A.G., 2005. Temperature of the upper mantel beneath the Intermontane Belt, northern Canadian Cordillera, determined from combining mineral composition, electrical conductivity laboratory studies and magnetotelluric field observations. Earth and Planetary Science Letters, 236, 258–268.
Lee, C-T.A., Lenardic, A., Cooper, C.M., Niu, F., Levander, A., 2005. The role of chemical boundary layers in regulating the thickness of continental and oceanic thermal boundary layers. Earth and Planetary Science Letters 230, 379–395.
Lehmann, I., 1960. Structure of the upper mantle as derived from the travel times of seismic P and S waves. Nature 186, 956.
Lehtonen, Marja L, O'Brien, H.E., Peltonen, P., Johanson, B.S., Pakkanen, L.K., 2004. Layered mantle at the Karelian Craton margin; *P–T* of mantle xenocrysts and xenoliths from the Kaavi-Kuopio kimberlites, Finland. Lithos 77, 593–608.
Lehtonen, M.L., Pakkanen, L.K., Johanson, B.S., 2005a. Electron microprobe and LA-ICP-MS analyses of garnet xenocrysts from Kaavi-Kuopio area kimberlites. Geological Survey Finland Open File. M41.2/2005/1.
Lehtonen, M.L., Pakkanen, L.K., Johanson, B.S., Lallukka, H.M., 2005b. EMP analyses of kimberlite indicator minerals from Pipe 7 and Dyke 16 kimberlites and the basal till surrounding them. Geological Survey Finland Open File. M41.2/2005/2.
Li, A., Forsyth, D.W., Fischer, K.M., 2003. Shear velocity structure and azimuthal anisotropy beneath eastern North America from Rayleigh wave inversion. Journal of Geophysical Research 108, 2362. doi:10.1029/2002JB002259.
Li, X., Kind, R., Yuan, X., Wolbern, I., Hanka, W., 2004. Rejuvenation of the lithosphere by the Hawaiian plume. Nature 427, 827–829.
Li, A., Burke, K., 2006. Upper mantle structure of southern Africa from Rayleigh wave tomography. Journal of Geophysical Research 111, B10303. doi:10.1029/2006JB004321.
Lizarralde, D., Chave, A., Hirth, G., Schultz, A., 1995. Northeastern Pacific mantle conductivity profile from long-period magnetotelluric sounding using Hawaii-to-California submarine cable data. Journal of Geophysical Research 100, 17,837–17,854.
Mackwell, S.J., 1991. High-temperature rheology of enstatite; implications for creep in the mantle. Geophysical Research Letters 18, 2027–2030.
Michaut, C., Jaupart, C., Bell, D.R., 2007. Transient geotherms in Archean continental lithosphere: new constraints on thickness and heat production of the subcontinental lithospheric mantle. Journal of Geophysical Research 112, B04408. doi:10.1029/2006JB004464.
Miensopust, M., Jones, A.G., Garcia, X., Muller, M., Hamilton, M.P., Spratt, J.E., Evans, R.L., Evans, S.F., Mountford, A., Fourie, C.J.S., Hutchins, D., Ngwisanyi, T., SAMTEX Team, 2006. Lithospheric studies of major Archean cratons and their Proterozoic bounding belts in southern Africa using MT. British Geophysical Association Postgraduate Meeting. Edinburgh. 31 August – 1 September 2006.
Mierdel, K., Keppler, H., Smyth, J.R., Langenhorst, F., 2007. Water solubility in aluminous orthoyroxene and the origin of Earth's asthenosphere. Science 315, 364–368.
Nickel, K.G., Green, D.H., 1985. Empirical geothermobarometry for garnet peridotites and implications for the nature of the lithosphere, kimberlites and diamonds. Earth and Planetary Science Letters 73, 158–170.

Nimis, P., Taylor, W.R., 2000. Single clinopyroxene thermobarometry for garnet peridotites. Part 1. Calibration and testing of a Cr-in-cpx barometer and enstatite-in-cpx thermometer. Contributions to Mineralogy and Petrology 139, 541–554.
O'Reilly, S.Y., Griffin, W.L., 2006. Imaging global chemical and thermal heterogeneity in the subcontinental lithospheric mantle with garnets and xenoliths: geophysical implications. Tectonophysics 416, 289–309.
Pearson, N.J., O'Reilly, S.Y., Griffin, W.L., 1995. The crust–mantle boundary beneath cratons and craton margins: a transect across the south-west margin of the Kaapvaal Craton. Litho 36, 257–287.
Pearson, N.J., Griffin, W.L., Doyle, B.J., O'Reilly, S.Y., Van Achterbergh, E., Kivi, K., 1999. Xenoliths from kimberlite pipes of the Lac de Gras area, Slave Craton, Canada. In: Gurney, J.J., Gurney, J.L., Pascoe, M.D., Richardson, S.H. (Eds.), J. B. Dawson Volume, Proceedings of the 7th International Kimberlite Conference. Red Roof Design, Cape Town, pp. 644–658.
Pedersen, H.A., Bruneton, M., Maupin, V., SVEKALAPKO Seismic Tomography Working Group, 2006. Lithospheric and sublithospheric anisotropy beneath the Baltic shield from surface wave array analysis. Earth and Planetary Science Letters 244, 590–605.
Plomerova, J., Kouba, D., Babuska, V., 2002. Mapping the lithosphere–asthenosphere boundary through changes in surface-wave anisotropy. Tectonophysics 358, 175–185.
Pollack, H.N., Chapman, D.S., 1977. On the regional variation of heat flow, geotherms, and lithospheric thickness. Tectonophysics 38, 279–296.
Pontevivo, A., Thybo, H., 2006. Test of the upper mantle low-velocity layer in Siberia with surface waves. Tectonophysics 416, 113–131.
Praus, O., Pecova, J., Petr, V., Babuska, V., Plomerova, J., 1990. Magnetotelluric and seismological determination of the lithosphere–asthenosphere transition in central Europe. Physics of the Earth and Planetary Interiors 60, 212–228.
Priestley, K., Debayle, E., 2003. Seismic evidence for a moderately thick lithosphere beneath the Siberian Platform. Geophysical Research Letters 30, 1118. doi:10.1029/2002GL015923.
Priestley, K., McKenzie, D., 2006. The thermal structure of the lithosphere from shear wave velocities. Earth and Planetary Science Letters 244, 285–301.
Priestley, K., McKenzie, D., Debayle, E., 2006. The state of the upper mantle beneath southern Africa. Tectonophysics 416, 101–112.
Ritsema, J., van Heijst, H., 2000. New seismic model of the upper mantle beneath Africa. Geology 28, 63–66.
Rümpker, G., Ryberg, T., 2000. New "Fresnel-zone" estimates for shear-wave splitting observations from finite-difference modelling. Geophysical Research Letters 27, 2005–2008.
Russell, J.K., Dipple, G.M., Kopylova, M.G., 2001. Heat production and heat flow in the mantle lithosphere, Slave Craton, Canada. Physics of the Earth and Planetary International 123, 27–44.
Rychert, C.A., Fischer, K.M., Rondenay, S., 2005. A sharp lithosphere–asthenosphere boundary imaged beneath eastern North America. Nature 436, 542–545.
Sacks, I.S., Snoke, J.A., 1977. The use of converted phases to infer the depth of the lithosphere–asthenosphere boundary beneath South America. Journal of Geophysical Research 82, 2011–2017.
Sacks, I.S., Snoke, J.A., Husebye, E.S., 1979. Lithosphere thickness beneath the Baltic shield. Tectonophysics 56, 101–110.
Saltzer, R., 2002. Upper mantle structure of the Kaapvaal craton from surface wave analysis — a second look. Geophysical Research Letters 29, 1093. doi:10.1029/2001GL013702.
Sandoval, S., Kissling, E., Ansorge, J., 2004. High-resolution body wave tomography beneath the SVEKALAPKO array — II. Anomalous upper mantle structure beneath the central Baltic Shield. Geophysical Journal International 157, 200–214.
Sebai, A., Stutzmann, E., Montagner, J.-P., Sicilia, D., Beucler, E., 2006. Anisotropic structure of the African upper mantle from Rayleigh and Love wave tomography. Physics of the Earth and Planetary Interiors 155, 48–62.
Shapiro, S.S., Hager, B.H., Jordan, T.H., 1999. The continental tectosphere and Earth's long-wavelength gravity field. Lithos 48, 135–152.
Silver, P.G., Fouch, M.J., Gao, S.S., Schmitz, M.D., 2004. Seismic anisotropy, mantle fabric, and the magmatic evolution of Precambrian Southern Africa. South African Journal of Geology 107, 45–58.
Simons, F.J., van der Hilst, R.D., 2002. Age-dependent seismic thickness and mechanical strength of the Australian lithosphere. Geophysical Research Letters 29, 1529. doi:10.1029/2002GL014962.
Simons, F.J., van der Hilst, R.D., Montagner, J.-P., Zielhuis, A., 2002. Multimode Rayleigh wave inversion for heterogeneity and azimuthal anisotropy of the Australian upper mantle. Geophysical Journal International 151, 738–754.
Smith, D., 1999. Temperatures and pressures of mineral equilibration in peridotite xenoliths: Review, discussion and implications. In: Fei, Y., Bertka, C.M., Mysen, B.O. (Eds.), Mantle Petrology: Field Observations and High Pressure Experimentation: A Tribute to Francis R. (Joe) Boyd. Geochemical Society Special Publication, 6, pp. 3–12.
Smith, D., Boyd, F.R., 1989. Compositional heterogeneities in minerals of sheared lherzolite inclusions from African kimberlites. Geological Society of Australia Special Publication 14, 709–724.
Sodoudi, F., Yuan, X., Liu, Q., Kind, R., Chen, J., 2006. Lithospheric thickness beneath the Dabie Shan, central eastern China from S receiver functions. Geophysical Journal International 166, 1363–1367.
Snoke, J.A., Sacks, I.S., Okada, H., 1977. Determination of the subducting lithosphere boundary by use of converted phases. Bulletin of the Seismological Society of America 67, 1051–1060.
Snyder, D., Bruneton, M., 2007. Seismic anisotropy of the Slave craton, NW Canada, from joint interpretation of SKS and Rayleigh waves. Geophysical Journal International 169, 170–188.
Sobolev, N.V., Lavrent, ' ev, Y.G., Pokhilenko, N.P., Usova, L.V., 1973. Chrome-rich garnets from the kimberlites of Yakutia and their parageneses. Contributions to Mineralogy and Petrology 40, 39–52.
Stubley, M.P., 2004. Spatial distribution of kimberlite in the Slave craton, Canada: a geometrical approach. Lithos 77, 683–693.
Taylor, W., 1998. An experimental test of some geothermometer and geobarometer formulations for upper mantle peridotites with application to the thermobarometry of fertile lherzolite and garnet websterite. Neues Jahrbuch Fuer Mineralogie Abhandlungen 172, 381–408.
ten Grotenhuis, S.M., Drury, M.R., Spiers, C.J., Peach, C.J., 2005. Melt distribution in olivine rocks based on electrical conductivity measurements. Journal of Geophysical Research 110, B12201. doi:10.1029/2004JB003462.
Vinnik, L.P., 1977. Detection of waves converted from P to SV in the mantle. Physics of the Earth and Planetary Interiors 15, 39–45.
Waff, H.S., 1974. Theoretical considerations of electrical conductivity in a partially molten mantle and implications for geothermometry. Journal of Geophysical Research 79, 4003–4010.
Walker, A.M., Hermann, J., Berry, A.J., O, ' Neill, H.S.C., 2007. Three water sites in upper mantle olivine and the role of titanium in the water weakening mechanism. Journal of Geophysical Research 112, B05211. doi:10.1029/2006JB004620.
Wang, D., Mookherjee, M., Xu, Y., Karato, S., 2006. The effect of water on the electrical conductivity of olivine. Nature 443, 977–980.
Weeraratne, D.S., Forsyth, D.W., Fischer, K.M., 2003. Evidence for an upper mantle plume beneath the Tanzanian craton from Rayleigh wave tomography. Journal of Geophysical Research 108, 2427. doi:10.1029/2002JB002273.
Xu, Y., Shankland, T.J., Poe, B.T., 2000. Laboratory-based electrical conductivity of the Earth's mantle. Journal of Geophysical Research 105, 27,865–27,875.
Yoshino, T., Manthilake, G., Nishi, M., Katsura, T., 2006. Electrical conductivity of mantle minerals. Eos, Transactions, American Geophysical Union 87, MR21A-0002.
Yuan, X., Kind, R., Li, X., Wang, R., 2006. The S receiver functions: synthetics and data example. Geophysical Journal International 165, 555–564.